Myelin Deficits and Intravenous Gene Therapy in Feline Sandhoff Disease

by

Anne Sessa Maguire

A dissertation submitted to the Graduate Faculty of
Auburn University
in partial fulfillment of the
requirements for the Degree of
Doctor of Philosophy

Auburn, Alabama
August 7, 2021

Keywords: Myelin, AAV Gene Therapy, GM2 gangliosidosis, Sandhoff Disease, Tay-Sachs Disease

Approved by

Douglas Martin, Chair, Professor of Anatomy, Physiology, & Pharmacology
Edward Morrison, Professor of Veterinary Histology and Neuroscience Emeritus
Robert Judd, Professor of Pharmacology
Eleanor Josephson, Associate Professor of Neuroscience and Anatomy
Emily Graff, Assistant Professor of Pathobiology

Abstract

Sandhoff Disease (SD) is a neurodegenerative lysosomal storage disease (LSD) that results in the death of children before 4 years of age. Because there are no FDA-approved therapies available, current treatment strategies are limited to palliation. SD is a form of GM2 gangliosidosis caused by the absence of ß-hexosaminidase (Hex) and subsequent accumulation of GM2 ganglioside in neuronal lysosomes. In previous studies, intracranial administration of adeno-associated viral (AAV) vector in feline models quadrupled lifespan and increased quality of life. To maximize patient benefit, and because gene therapy manufacturing is expensive and labor-intensive, it is crucial to make sure that each dose is as effective as possible.

Chapter 1 of this dissertation investigated the possibility of using a bicistronic AAV vector, reducing the risk of intracranial surgery, and achieving greater systemic vector distribution through the intravenous (IV) treatment of SD cats at one month of age. In-life assessments revealed clear clinical benefit of AAV treatment, with the most dramatic improvement seen in the reduction of tremors, the most debilitating feature of feline SD. Other *in vivo* metrics were measured in cerebrospinal fluid and utilizing magnetic resonance imaging; these revealed partial normalization of AAV-treated cats, with the high dose being more effective than the low dose. Post-mortem assessments revealed dose-dependent reduction of GM2 ganglioside storage and increases in Hex activity that were more substantial in the caudal regions of the brain and in the spinal cord. Immunohistochemistry (IHC) staining revealed partial normalization for 4

separate cell populations (astrocytes, microglia, neurons, oligodendrocytes). The brainstem was the region with the mildest pathology after AAV treatment, along with the spinal cord when included. These results support the dose-dependent efficacy of AAV delivered IV in a feline model of SD.

Chapter 2 addressed current gaps in the literature on the origin of myelin deficits in SD, which is increasingly recognized as a barrier to effective gene therapy in multiple LSDs. Myelin pathology was characterized in SD cats by measuring mRNA and protein (IHC) markers of myelinogenesis at 3-4 different stages of feline development. Deficits were noted as early as 1 month of age, which is considered pre-symptomatic. As previously reported in humans and mice, the feline brainstem was one of the first areas to become myelinated in normal cats. These results accentuate the importance of intervening with AAV treatment as early as possible, though the diagnosis of pre-symptomatic children is difficult and rare.

Acknowledgements

I would like to thank my advisor and mentor Douglas R. Martin for his support over my eight-year academic career at Auburn University. I have learned so much about leadership, science, and maintaining a special environment where research is both enjoyable and impactful. I could not imagine completing a PhD program anywhere else.

I would also like to thank my committee members Edward Morrison, Robert Judd, Eleanor Josephson, and Emily Graff for their valuable advice and support. All of the faculty members at Auburn University that have taught, mentored, and supported me throughout the DVM and PhD curricula have molded me into the knowledgeable, confident, and thoughtful veterinarian-researcher I am today. I would not have nurtured my interest in neuropathology without the infectious enthusiasm of Brandon Brunson, persisted in my efforts to join the Martin lab without the wise counsel of Elaine Coleman, or built upon my passion for image analysis without the unflagging encouragement of Emily Graff.

All of the current and past members of the Martin and Baker labs have made important contributions towards making the dream of treating terminally ill children a reality. In particular, I would like to thank Jessica Cannon for ensuring that every member of the cat colony is treated with care and compassion, Heather Gray-Edwards for developing the MRI protocol I used, and my office-mate Allisandra Rha for her boundless companionship, encouragement, and support.

My heartfelt gratitude to my family, Gale Sessa, Wade Maguire, and Bo Maguire, for always looking out for my best interests, always picking up the phone when I call, and sometimes humoring my puns and long-winded scientific explanations over fantastic dinners. Thank you to my loving partner Chris Gorman for making the bad times less bad and the good times more good.

This work was supported by the National Institute of Health grant R01 NS09341 and the Center for Neuroscience Initiative Graduate Fellow Program at Auburn University.

Table of Contents

List of Tables

Literature Review

Chapter 1

List of Figures

Literature Review

Chapter 1

Chapter 2

List of Abbreviations

4-MU	4-methylumbelliferyl
AAV	Adeno-associated virus
ßgal	ß-galactosidase
CNS	Central nervous system
CRS	Clinical rating score
CSF	Cerebro-spinal fluid
DCN	Deep cerebellar nuclei
GalC	Galactocerebroside
GFAP	Glial fibrillary acidic protein
GM1	GM1 gangliosidosis
GM2	GM2 gangliosidosis
GPC+PCh	Glycerophosphocholine + phosphocholine
H&E	Hematoxylin & Eosin
Hex	ß-N-acetylhexosaminidase
HPTLC	High-performance thin layer chromatography
Iba-1	Ionized calcium-binding adaptor molecule 1
ICV	Intracerebroventricular
IHC	Immunohistochemistry
Ins	Myoinositol
IV	Intravenous
KD	Krabbe Disease
LFB	Luxol Fast Blue

LSD	Lysosomal storage disease
MAG	Myelin-associated glycoprotein
MBP	Myelin basic protein
MRI	Magnetic resonance imaging
MRS	Magnetic resonance spectroscopy
NG2	Neural-glial antigen 2
OPC	Oligodendrocyte precursor cell
PDGFRA	Platelet-derived growth factor receptor – alpha
PLP1	Proteo-lipid protein 1
SD	Sandhoff Disease
TEM	Transmission electron microscopy
TSD	Tay-Sachs Disease

Literature Review

1. Introduction

GM2 gangliosidosis (GM2) is a devastating lysosomal storage disease (LSD) that results in the neurodegenerative decline and death of children before 4 years of age. Dysfunction of the lysosomal enzyme ß-N-acetylhexosamimidase (Hex) is inherited in an autosomal recessive pattern, resulting in the buildup of GM2 ganglioside in neuron cell bodies. Three clinically similar subtypes of GM2 exist: Tay-Sachs disease (TSD), Sandhoff disease (SD), and GM2 activator deficiency. While TSD and SD affect one in 200,000 to 400,000 live births[1], GM2 activator deficiency occurrence has only been recorded in a handful of cases across the world.

Regardless of genetic origin, dysfunction of Hex enzymes causes a cascade of central nervous system (CNS) symptoms in affected patients such as delay or loss of developmental milestones, difficulty swallowing, seizures, and ultimately death. Currently, only palliative treatment is approved by the FDA, but clinical trials with gene therapy began in 2021 and provide new hope for patients and their families. Gene therapy involves the delivery of a dysfunctional gene, typically through a viral vector. The animal studies that preceded clinical trials have shown dramatic improvement in clinical metrics, but complete normalization has yet to be achieved reproducibly. To maximize patient benefit, and because gene therapy manufacturing is expensive and labor-intensive, it is crucial to make sure that each dose is as effective as possible.

While gene therapy usually results in enzyme activity at or above effective levels (10-20% of normal) and substantially reduced neuronal storage, lifespans and other measures of success are still not at normal levels. This leads researchers to suspect that other deficits persist despite gene therapy, such as inflammation and myelin pathology. Indeed, white matter deficits are increasingly considered therapeutic targets in neurodegenerative diseases such as Alzheimer's disease[2], Parkinson's disease[3], and other closely related LSDs[4-6]. Similarly, white matter pathology in GM2 has been characterized since the 1970s and is now receiving attention as a phenomenon potentially separate from gray matter deficits. While early gene therapy efforts focused on enzyme activity restoration and storage reduction, recent studies have implied that myelin pathology is at least partially refractory to gene therapy. Therefore, to improve the efficacy of treatment, the field would benefit from future gene therapy studies incorporating white matter metrics.

The objective of this dissertation is to assess the efficacy of a new gene therapy treatment and characterize myelin deficit pathogenesis in a feline model of SD. The overlapping areas of study encompassed by this dissertation are depicted in Figure 1. Intravenous delivery of a novel bicistronic adeno-associated viral (AAV) vector will be evaluated in Chapter 1, which will include an assessment of how well AAV treatment corrects white matter pathology in SD cats. Chapter 2 contrasts the normal development of myelin in immature cats with the concurrent pathogenesis of SD. Both studies utilize whole-slide image analysis, an innovative method for quantification of immunohistochemistry (IHC) staining, which is described in detail in Chapter 1. By establishing standardized metrics for white matter assessment in a large-scale gene therapy study, this work advances the field of translational medicine for devastating neurodegenerative diseases.

2. GM2 gangliosidosis

2.1 Lysosomal storage diseases

First described in 1955 by Christian de Duve, lysosomes are organelles that degrade much of a cell's waste material through a variety of hydrolytic enzymes (hydrolases)[7]. The LSD family consists of more than 50 distinct metabolic disorders, most of which result from the deficiency of specific hydrolases. Most LSDs have severe CNS manifestations, and mild CNS disease is now recognized in many LSDs previously thought to be non-neurologic. Figure 2 outlines normal catabolic pathways and the diseases caused by dysfunction of specific hydrolases[8]. These pathways are so closely related that dysfunction in one enzyme often results in a compensatory increase in activity of enzymes with similar functions, though the overall goal of reducing storage material may not be accomplished. Of note is the fact that ß-galactosidase (deficient in GM1 gangliosidosis) is one catabolic step away from Hex, and therefore the resulting disease GM1 gangliosidosis has a similar clinical phenotype to GM2.

2.2 Biochemistry

The biochemical differences between subtypes of GM2 is partially due to the combination of 2 subunits (α and ß) into 3 distinct dimeric isozymes: HexA (αß), HexB (ßß), and HexS ($\alpha\alpha$)[9]. In humans, HexA degrades GM2 ganglioside and its asialo derivative GA2 ganglioside, HexB degrades only GA2 ganglioside, while HexS is unstable and does not play a significant role in substrate reduction. The homozygous mutation of *HEXA* genes (TSD) results in dysfunction of the α subunit and subsequently HexA, while mutation of *HEXB* (SD) causes functional loss of the ß subunit and therefore HexA and HexB. For therapeutic purposes, both subunits must be expressed even though only one is missing because over-expression of the α or β subunit alone leads to preferential assembly of HexS or HexB, respectively, neither of which contribute to GM2 ganglioside degradation in humans. Also, the isozyme assembly process would otherwise lead to excessive degradation of single subunits. Subunits are assembled into isozymes in the endoplasmic reticulum, then transported to the lysosomes[10]. Therefore, subunits that arrive at the endoplasmic reticulum at different times risk being degraded before being assembled with their “partner”, and low efficiency of isozyme production. This issue is only applicable to HexA, since two different subunits (α and ß) must be present in approximately equal ratios.

Though TSD and SD are often considered clinically indistinguishable in human patients, their biochemical differences play a role in animal models. Mice possess an alternate catabolism pathway that uses sialidase to degrade GM2 ganglioside to GA2 ganglioside[11]. Mice that still have functional HexB (TSD models) use sialidase to degrade GM2 ganglioside to GA2 ganglioside. Then, a unique GM2 activator protein functionality in mice (that is not present in humans) permits HexB to break down GA2 ganglioside, substantially reducing storage of GM2 ganglioside and the resulting pathological phenotype. In contrast, SD mice (missing both HexA and HexB) cannot break down either GM2 or GA2 ganglioside, resulting in pathology that can be loosely compared to human patients[11]. Because humans do not possess the alternate catabolism pathway, they must rely only on HexA for breakdown of GM2 ganglioside, and the identity of the missing subunit (α or ß) becomes less relevant.

2.3 Clinical disease progression

There are 3 clinical manifestations of GM2 gangliosidosis: infantile, juvenile, and late-onset. Infantile is the most common and severe form, with mean age at symptom onset of 5.0$\underline{+}$3.3 months followed by rapid progression of neurologic symptoms including exaggerated startle response, seizures, diminished eyesight, and spasticity[12]. Despite intense supportive care, including insertion of gastric feeding tubes and suctioning of mucous/oral secretions, most patients die before they are 4 years old[12]. Juvenile GM2 cases have a mean age of symptom onset at 5.3$\underline{+}$4.1 years with gait disturbances and incoordination, followed by a progression of neurologic symptoms that could include muscle wasting, proximal weakness, and incontinence before death at 14.5 years (median)[13]. Symptoms of late-onset GM2 (often TSD) can manifest from adolescence to 20-30 years old, with a slower neurologic decline that includes motor and psychiatric abnormalities[14]. The heterogeneity between and within these 3 variances is attributed to differential residual HexA activity based on mutation type, ranging from <0.5% for infantile and 5-20% for late-onset patients[14].

2.4 Pathology

The accumulation of GM2 ganglioside in neurons forms characteristic inclusions (known as membranous cytoplasmic bodies) as well as a pathological cascade throughout the CNS and peripheral tissues. The macular cherry-red spot, a typical clinical sign in infants, is caused by the contrast between a normal portion of retina and the surrounding white areas filled with storage products[7]. The cerebrum, pons, medulla, and spinal cord are atrophic, with storage material commonly found in neurons and microglia upon ultrastructural examination[7]. Thickened aortic and mitral valve leaflets appear concurrently with storage-filled cardiac histiocytes, while foamy macrophages are found throughout the bone marrow. Ganglia within the gastrointestinal tract are also swollen with storage material[7]. However, the liver, spleen, and lymph nodes appear within normal limits grossly and microscopically[7].

In addition to the primary disease process of ganglioside storage, two other neuropathologies occur: myelin deficits (covered in detail in section 4) and inflammation. Extensive microglia activation has been described in both humans[15] and mice[16], with a massive neuronal death event following in mice[15]. Infiltration of inflammatory cells and altered blood brain barrier permeability coincide with the onset of clinical signs in SD mice[16]. Inflammatory biomarkers found in the CSF of infantile patients (ENA-78, MCP-1, MIP-1α, MIP-1ß, and TNFR2) have been proposed as biomarkers for monitoring disease progression and therapeutic effects[17].

2.5 Feline model

First described in the 1970s[18,19], the feline model of SD is a valuable intermediate model between mice and humans. The causative mutation is a 25-base-pair inversion at the 3’ end of *HEXB*, resulting in 3 amino acid substitutions and a premature translational stop[20]. Due to their rapid neurological disease progression and very little residual HexA activity throughout the CNS, these cats are representative models of the infantile form of SD. While the SD mouse is excellent for investigating a barrage of therapies where quick turnover is necessary, the SD cat is more appropriate for testing long-term therapeutics that are expected to directly translate to human clinical trials. The size and complexity of the feline brain more faithfully represents the human brain, and the expected longevity of cats allows the investigation of the long-term impact of potential therapeutics. In addition, SD cats are the result of a naturally occurring mutation (as opposed to mice which are created by completely knocking out *HEXB*) and therefore represent the biochemistry of human SD more accurately.

2.5.1 CNS pathology in the feline model

Clinical metrics of CNS disease progression have been well-characterized in the SD cat and are valuable tools to compare disease progression and therapeutic response to human patients. The most pronounced clinical sign in SD cats is overt whole-body tremors, which progress rapidly until the cats reach a predetermined humane endpoint at 4.2±0.3 months (inability to stand for 2 consecutive days). Proprioceptive deficits are a common development late in disease progression. T2-weighted MR (magnetic resonance) images acquired at humane endpoint reveal hypointense gray matter, hyperintense white matter, and increased cerebrospinal fluid (CSF) signal between the brain parenchyma and meninges[21]. CSF can also be collected and evaluated directly, with high levels of AST and LDH in SD cats indicating CNS cell damage[21].

Post-mortem, swollen neurons suggestive of storage are visible within neurons on Hematoxylin & Eosin (H&E) stained slides as well as with transmission electron microscopy (TEM). Also visible on TEM are neuroaxonal spheroids and digestion chambers, indications of a pathological cascade that may be downstream of the storage deficits (unpublished data). Other indicators of lipid-based storage material throughout the CNS include intense Periodic Acid-Schiff (PAS) staining and increased GM2 and GA2 ganglioside when quantified by high-performance thin layer chromatography (HPTLC)[22,23]. These storage deficits correlate with decreased HexA activity, as measured by 4-methylumbelliferyl (4-MU) assays and visualized by naphthol staining[22,23]. An indirect marker of decreased HexA activity is the increased activity of other lysosomal enzymes (ß-galactosidase and mannosidase), thought to be a compensatory response to high levels of storage material[22,23]. Inflammatory processes are evident throughout the CNS in SD cats, including microglia activation and astrocyte proliferation[24]. Myelin pathology is also evident throughout the CNS and will be discussed in detail in section 4.

2.5.2 Peripheral pathology in the feline model

Facial features of SD cats are coarse when compared to age-matched normal controls, and include shortened muzzles, flattened skulls, smaller ears, and opaque corneas[25]. Bony lesions are evident upon radiological examination of the cervical spine and coxofemoral region[25]. Upon histologic examination of bone, fewer chondrocytes and osteoblasts are found in SD cats, with storage material present in the chondrocytes that are present[25]. By 4 months of age, SD cats have a substantially larger aorta than their normal counterparts, as measured by echocardiography[25]. Postmortem, great vessel valve leaflets and walls are thickened in SD cats, consisting of fibroblasts swollen with alcianophilic-staining storage material[25]. These cardiac changes are similar to those found in human SD patients, who display cardiomegaly, left ventricular hypertrophy, and thickened valves[25]. Gastrointestinal signs in SD cats are apparent on ultrasound and include stomach and bladder distension, intestinal wall thickening, fibrous liver parenchyma, and bile duct distension/obstruction (unpublished data).

3. Normal Myelinogenesis

3.1 Oligodendrocyte physiology

Oligodendrocytes are the glial cells responsible for myelination of the CNS. During embryonic development, their progenitor cells (oligodendrocyte precursor cells, OPCs) proliferate in and migrate from the germinal zones of the neural tube throughout the gray and white matter. Though most OPCs mature into myelin-producing oligodendrocytes, a substantial number are maintained as precursors in the adult CNS, which is an unusual characteristic for progenitor cells[26]. These OPCs generate mature oligodendrocytes, which in turn are known to play important roles in remyelination after CNS damage and myelin plasticity in response to life experiences (a process known as “adaptive” myelination)[26].

Oligodendrocytes have four developmental stages: oligodendrocyte precursor cell (OPC), preoligodendrocyte, immature oligodendrocyte, and mature oligodendrocyte (Figure 3)[27]. Common protein markers used for identification of these stages include NG2 (neural glial antigen 2) and PDGFRA (platelet-derived growth factor receptor α) for OPCs and preoligodendrocytes, with the additional expression of O4 and GRP17 marking a transition between the two cell types. O4 expression is retained by immature oligodendrocytes, which also produce GalC (galactocerebroside) and CNPase (2′,3′-cyclic nucleotide 3′-phosphodiesterase). MBP (myelin basic protein), PLP1 (proteo-lipid protein 1), and MAG (myelin-associated glycoprotein) are markers of mature oligodendrocytes[27]. In humans, this process is initiated at 10 weeks post-conception when OPCs first appear, and it reaches completion perinatally with the appearance of substantial numbers of MBP-positive mature oligodendrocytes[27]. Olig2 is essential for oligodendrocyte maturation and expressed throughout these developmental stages, while Olig1 is considered more important for remyelination processes[26].

3.2 Myelin Sheath Assembly

The primary function of lipid-rich myelin sheaths is to accelerate the transmission of action potentials down axons, and these structures are therefore critical for signals that need to travel quickly, such as those involved in specialized sensory and motor pathways. The production and subsequent maintenance of a mature myelin network is extremely energy consuming (though presumably worth the tradeoff of increased action potential speed), and therefore myelin synthesis proceeds in a careful, highly regulated manner[28]. Myelin sheath components include specific families of lipids in addition to the proteins present on the mature oligodendrocyte cell membrane (such as MBP and PLP). In humans, the appearance of these substances follows a prescribed sequence consisting of major lipids and proteins that can be detected biochemically. Cholesterol synthesized by oligodendrocytes is a critical precursor of myelin sheaths and a rate-limiting factor in their formation[29]. Myelinating oligodendrocytes produce galactosylceramide (GalCer) in the ER, which can have a sulfate group added in the Golgi apparatus to form sulfatides[30]. Formation of phospholipids precedes the emergence of sphingomyelin, which is followed by the near-simultaneous appearance of cerebrosides, sulfatides, MBP and PLP. The latter four substances are the primary components of adult myelin[31]. The onset of this sequence varies substantially between anatomical regions, but ranges from mid-gestation (for the tracts that are the earliest to myelinate) to early infancy (for the later-developing tracts)[31].

3.3 Axonal Communication

Recent evidence has revealed that neuroaxonal communication with oligodendrocytes and myelin sheaths is critical to the development of mature myelin and the maintenance of plastic neuronal circuitry[32-34]. Indeed, emerging concepts such as activity-dependent myelination and the existence of an axomyelinic synapse (as reviewed in Chorgay et al., 2018[34]) imply that axonal interactions must be considered when investigating oligodendrocyte and myelin development. For example, glutamate released from axons after action potentials likely binds to receptors on both OPCs and oligodendrocytes, with the former hastening OPC maturation and the latter facilitating myelin sheath plasticity and maintaining CNS circuitry[34]. Still undergoing active research is the timing of activity-dependent myelination mechanisms, which appear to be highly variable throughout brain regions and developmental experiences. A detailed understanding of this concept would provide valuable insight into the pathology of diseases (such as GM2) with concurrent developmental and degenerative components.

4. White matter pathology in the gangliosidoses and Krabbe disease

White matter deficits have long been reported in GM2 gangliosidosis, with occasional speculation as to their origin. Because of the small amount of information in the literature about this topic, the myelin pathogenesis of GM2 will be discussed in tandem with that of GM1 and contrasted with Krabbe disease. GM1 results from the mutation of the *GLB1* gene, causing the dysfunction of ß-galactosidase (ßgal) and the buildup of neuronal GM1 ganglioside (the catabolic precursor to GM2 ganglioside). Krabbe disease, also known as globoid cell leukodystrophy, is caused by dysfunction of galactosylceramidase (GALC), which breaks down the myelin sphingolipid galactosylceramide (Figure 2) and leads to extensive white matter degeneration[30]. Unlike GM1 and GM2, the primary insult of Krabbe disease occurs in white matter, and therefore its comparison to the gangliosidoses sheds light on the way in which myelin pathology occurs.

There are three proposed mechanisms for how myelin deficits occur as part of any CNS pathology: dysmyelinogenesis (failure to form properly), primary demyelination (destruction after proper formation), or secondary demyelination (loss after axonal degeneration) (Figure 4). An emerging theme in the gangliosidosis literature suggests that dysmyelinogenesis is the main contributor to white matter pathology, with primary and secondary demyelination playing less important roles. Last reviewed by Folkerth in 1999[35], this hypothesis is supported by early deficits in white matter tract development and abnormal myelin sheath structure. A detailed understanding of the mechanism for myelin pathology remains elusive in the current literature, with evidence available to support interference with all major components of myelinogenesis: oligodendrocytes, myelin sheaths, and neuroaxonal complexes. The use of inducible mouse models of gangliosidosis, which permit shutdown of Hex expression at different ages, may provide insight into myelin pathogenesis at critical developmental stages[36].

4.1 Early Deficits in White Matter Tract Development

Though a generalized “loss of white matter” is routinely reported as part of the diagnostic process in case studies of the gangliosidoses, few publications examine these deficits in more detail to elucidate the timing of the onset of dysmyelinogenesis. The most common methods include magnetic resonance imaging (MRI) and histochemical staining (Weil or Luxol Fast Blue). In cat, dog, and sheep models of both GM1 and GM2, cerebellar and cerebral cortical white matter is universally considered decreased compared to normal counterparts[37-40], while results for non-cortical white matter are mixed. In GM1[41] and GM2[42] patients, tracts that would normally develop prenatally are less affected than tracts that develop postnatally, and therefore a perinatal onset of dysmyelinogenesis has been hypothesized for the gangliosidoses.

4.2 Abnormal Myelin Sheath Architecture

The myelin sheath in GM1 and GM2 has been critically evaluated from two perspectives: quantification of its major components and evidence of its breakdown (Table 1). The most thoroughly investigated myelin sheath components are cerebrosides and sulfatides, which have been shown via HPTLC to be decreased in CNS tissue across mice, dogs, cats, and human patients with both GM1 and GM2[23,38,42-47] (Table 1). Collectively, these studies implicate that such deficits occur in most major regions of the CNS. A notable exception was observed in Gray-Edwards et al. 2017[48], who found an increase in cerebrosides and sulfatides in cerebrospinal fluid (CSF) of cats with GM1, potentially indicating leakage due to myelin breakdown in the CNS parenchyma.

The consensus on cerebroside and sulfatide deficiencies in GM1 and GM2 leads to the question of whether there are similar changes in the major myelin proteins that emerge at the same time in normal myelinogenesis. Unfortunately, only two studies have investigated protein and mRNA levels for MBP, PLP, MAG, and CGT (UDP-galactose:ceramide galactosyltransferase), and more region-specific work is needed to draw concrete conclusions about the onset of white matter pathogenesis. For example, protein levels of MBP and PLP are decreased both in the frontal lobe of humans with GM1[49] and the cerebrum of mice with GM2[50], but no other regions have undergone quantitative analysis. The mRNA levels of MBP, MAG, and CGT in the olfactory bulb, cerebrum, cerebellum, brainstem, and spinal cord of GM2 mice were either at or below normal levels, with the only consistencies across all three markers occurring in the cerebrum (normal levels) or brainstem (below normal levels)[50].

Histological and ultrastructural assessments of myelin sheath integrity inconsistently note pathological changes (Table 1), but studies in animal models only examine one or two CNS regions at this level[37,40,43,51]. More informative are the comprehensive evaluations of autopsy cases of GM1[41] and GM2[42] patients that compared major CNS regions and white matter tracts. Both studies noted abnormally thin sheaths that were otherwise structurally intact. In GM2 patients, sudanophilic breakdown products were found throughout the CNS in a pattern that roughly corresponded with neuronal loss[42]. These breakdown products were presumed to be degenerating myelin and axons, prompting the proposed mechanism that secondary demyelination occurs after neuronal loss caused by storage or metabolic insults[42].

In conclusion, the evidence for early deficiencies in the major components of myelin with few indications of their destruction supports the hypothesis that dysmyelinogenesis is the predominant mechanism of gangliosidosis white matter pathology, with minor contributions from primary and/or secondary demyelination. This conclusion could be modified as more investigations are conducted into myelin proteins and sheath degeneration across CNS regions in animal models.

4.3 Oligodendrocyte Pathology

Pathological changes to oligodendrocytes have been found across species (Table 1), and CNS regions. Oligodendrocyte number is qualitatively decreased upon evaluation of limited regions of GM1 human tissue[41,49], but unchanged from normal levels when immunohistochemistry (IHC) staining is quantified throughout the brain of GM1 cats[40]. The only study to investigate oligodendrocytes in GM2 found a similar number in affected human patients compared to normal[42]. Evidence of oligodendrocyte cell injury is apparent in GM1 through TUNEL staining[49] or ultrastructural examination[40]. Despite these abnormalities in number and pathological changes, the consensus appears to be that ganglioside storage does not occur in oligodendrocytes[40,41,46,49], with the only exception reported in one Japanese spaniel with GM2[51]. Authors that observe oligodendrocyte pathology consider it to play a substantial role in the development of white matter deficits, but specific mechanisms of action and the extent of concurrent dysfunctional neuroaxonal communication have yet to be delineated.

4.4 Neuroaxonal Dystrophy

Neuronal pathology incited by ganglioside storage likely contributes to myelin pathology through deficiencies in axonal-oligodendrocyte communication, secondary demyelination, or both. While the separate concepts of neuroaxonal dystrophy in GM1/GM2 (Table 1) and axon-led activity-dependent myelination[34] are well-established in the literature, they have not been thoroughly investigated together as a potential mechanism for white matter deficits in the gangliosidoses. Common methods for investigating neuroaxonal pathology include quantitative IHC (NeuN stain), and qualitative evaluation of hematoxylin & eosin (H&E) staining, silver staining, and ultrastructure. In most species with gangliosidosis, myelinated and total numbers of axons are decreased[38,41,42,49]. This could be due to degenerative changes within axons, which are found inconsistently throughout the CNS[37-39,41,42,49-53], or secondary to the decrease in cell body number noted in mice with GM2[50,54]. Regardless of cause, the contribution of axonal loss to secondary demyelination and/or dysfunctional activity-dependent myelination represents an intriguing area of future study.

4.5 Krabbe Disease

Any discussion of white matter pathology in LSDs would be incomplete without inclusion of Krabbe Disease (KD), well-characterized for decades as an LSD with white-matter-centric pathology. KD, also known as globoid cell leukodystrophy (GLD), has been well-studied for years, not only to find a cure for its devastating effects, but also as a classic model of developmental demyelination. Indeed, the *twitcher* mouse model of KD (galactocerebrosidase dysfunctional[55]) was one of the first LSD and leukodystrophy models created, and has been used in almost 100 studies since its discovery in 1980[30]. In contrast to the majority of LSDs, the pathophysiology of KD is not primarily due to accumulation of the primary substrate of GALC (galactosylceramide, GalCer), which is even shown to decrease[56]. Instead, the cytotoxic substrate psychosine accumulates, causing a pathological cascade of oligodendrocyte loss, demyelination, and neuronal degeneration. Psychosine is hypothesized to act as a detergent that disturbs the cell membrane and lipid rafts, leading to cell death in oligodendrocytes, where it is primarily produced in addition to neurons and microglia that are unable to digest the damaged myelin efficiently[30]. Cytoplasmic membranes, swollen lysosomes, unique lipid crystals, and broken-down myelin sheaths build up in PAS-positive "globoid cells"[30].

The severity of myelination deficits in KD coincides with the spatio-temporal patterns of normal myelinogenesis. Structures in which myelination is completed later in infancy (anterior and lateral spinal columns) display moderate to severe demyelination, while structures that are typically myelinated at birth (dorsal columns) are only mildly affected[35]. This pattern is also followed by the appearance of globoid cells, in that sites with more myelin tubules display more inclusion cells. In *twitcher* mice, MBP, MAG, PLP, and CGT mRNA levels are comparable to age-matched control mice until 20 days of age (the age at which these levels peak in normal development)[35]. At this point, mRNA expression falls disproportionately, during the time in which myelination should be occurring during normal development[35]. After 45 days of age, the dominant pathological mechanism switches from dysmyelinogenesis to destruction of previously formed myelin through primary demyelination, with the myelin remnants accumulating in globoid cells[35]. Of note is that the pro-inflammatory marker toll-like receptor 2 (TLR2) is upregulated on macrophages and microglia in *twitcher* mice by 2 weeks of age[57] and GFAP (glial fibrillary acidic protein) mRNA levels increase before the onset of demyelination[35]. This counterintuitively implies that neuroinflammatory processes precede demyelination instead of being a reaction to the formation of globoid cells.

Direct comparisons between SD and *twitcher* mice were made by Cachon-Gonzalez et al. in 2014[50] with respect to both myelination deficits and neuroinflammation. Both disease models showed increased mRNA levels of the neuroinflammatory markers CD68, GFAP, and MIP-1α throughout the CNS[50].

The highest levels were found in the hindbrain and spinal cord, early-myelinating areas which are rich in white matter. Though examined as early as 5 weeks of age, CD68 and GFAP mRNA levels did not reach maximal levels until 13 weeks of age in SD, coinciding with the onset of clinical signs. This is in contrast with mRNA levels of CGT, which are abnormally low at 5 weeks of age. This implies that, unlike in *twitcher* mice, myelination deficits in SD mice precede neuroinflammation. Though there are clear differences between the pathophysiology of SD and KD, inclusion of KD in any myelin-centric neurodegenerative discussion is critical due to the extensive characterization of the white matter pathology of the disease and the *twitcher* mouse model.

5. Gene therapy in the gangliosidoses

5.1 Gene therapy

Gene therapy is the use of a vector (typically viral) to deliver nucleic acids to a patient. Because LSDs are typically the result of well-characterized, monogenic, loss-of-function mutations, gene therapy has revolutionized the field of LSD therapeutics by delivering functional copies of the defective genes. GM1 and GM2 gangliosidosis further benefit from gene therapy because lysosomal enzymes such as ßgal and HexA are naturally secreted from corrected neurons and taken up by neighboring ones, a process known as cross-correction. Because of cross-correction and the fact that only 20% of normal enzyme activity is needed for a normal phenotype, relatively few neurons need to be transduced to have a therapeutic effect. Creation of a viral gene therapy vector involves replacing the replication and capsid or envelope sections of a viral genome with the transgene of interest, appropriate promoter, and any other necessary regulatory elements. The most common viral vectors used in LSD therapeutics are retroviruses, lentiviruses, adenoviruses, and adeno-associated viruses (AAVs)[58]. Major considerations when selecting a viral vector include the packaging capacity (how large of a transgene it can accommodate), whether it integrates into the genome (potentially upregulating nearby oncogenes), and whether it incites an immune response. The most common viral vector used in the treatment of GM1 and GM2 gangliosidosis is AAV.

5.2 AAV vectors

AAVs are members of the non-enveloped Parvoviridae family and unable to replicate on their own. Unless there is a helper virus (such as adenovirus) present in the host cell, the AAV genome remains latent in an episomal state[58]. AAVs are not known to cause disease in humans, though the majority of the population has been exposed to wild-type AAV serotypes at some point in their lifetime[58]. The naturally occurring AAV genome contains replication (rep) and capsid (cap) genes, and is flanked by 145 base pair inverted terminal repeats (ITRs)[59]. The wild-type rep and cap genes are removed in recombinant AAV (rAAV) and replaced by a promoter, capsid, polyA tail, and sometimes a post-transcriptional regulatory element (PRE). Advantages to AAV over other vectors include the fact that it is non-integrating, non-pathogenic, and has relatively low immunogenicity (though T-cells have been shown to respond to the transgene)[58].

A disadvantage to AAV is that its packaging capacity can only accommodate transgenes up to 4.7Kb, approximately half as much as retroviruses and adenoviruses can hold[58].

One recent advance in gene therapy for GM2 is the development of bicistronic AAV vectors. Monocistronic vectors express either the α or ß subunit of HexA and are typically mixed in a 50:50 ratio in the mixture given to the subject. However, this method runs the risk of individual monomers being degraded before they reach the ER and complete the dimerization process[9,10]. Co-expression of both the α and ß subunits within a given transfected cell leads to optimal cellular production of HexA before either subunit has a chance to be depleted. Because transit in the blood or CSF from the injection site leads to substantial vector dilution effects, the probability is low that a given cell is transfected by two separate AAVs, each expressing a different subunit. Therefore, the emergence of a single bicistronic construct that ensures the co-expression of both Hex subunits is a critical development in the advancement of gene therapy for SD[60], and is featured in chapter 2 of this dissertation.

5.3 Therapeutic efficacy of AAV in the gangliosidoses

Gene therapy for GM2 and the closely related GM1 has achieved outstanding preclinical results using several vector backbones, capsids, delivery routes, and animal models (Table 2)[61-63]. Initial studies in the gangliosidoses involved lentivirus and adenovirus[64-68], but many recent studies focus on AAV. Intracranial administration sites included the striatum or thalamus with or without the cerebellum[22,45,50,54,69-72], structures with important functional roles that are generally well connected with other regions of the CNS. Concerns about the risk of cerebellar surgery in affected children led to studies that substituted the lateral ventricle (intracerebroventricular, ICV) for cerebellum injection sites[23,40,73]. Recently, injections of the cisterna magna and/or intravenous routes have shown promising results and led to clinical trials in humans. Taghian et al. (2020)[74] recently described a novel technique for administering vector intrathecally in two TSD patients as part of an expanded access trial. Also, a phase I/II clinical trial for GM2 gangliosidosis (ClinicalTrials.gov Identifier NCT04669535) and three trials for GM1 (NCT03952637; NCT04713475; NCT04273269) children are underway or almost so.

The degree of lifespan extension in AAV-treated animals often correlates with other metrics used to evaluate gene therapy success. Common avenues of investigation include enzyme activity, ganglioside storage, lipid content, inflammatory response, and other histopathological changes. These assessments are also often used to investigate potential mechanisms of gangliosidosis pathogenesis. Recently, biomarkers such as neurological status, MRI, MRS, CSF, and blood chemistry markers have emerged as valuable tools for assessing treatment effectiveness in-life[21,75,76]. Some of these biomarkers correlate well between human patients and animal models, and are therefore expected to play important roles in clinical trials[75].

6. Gene therapy and myelin in the gangliosidoses

Though supporting evidence is needed, investigations into white matter deficits within gene-therapy treated animal models of the gangliosidoses imply that myelin deficits are refractory to gene therapy treatment. Cachon-Gonzalez et al. (2014)[50] found that myelin protein content in treated SD mice remained abnormally low regardless of age at treatment and petitioned for further investigation with a larger cohort of animals. However, early treatment did seem to provide the best opportunity to preserve myelin. SD mice treated at 12 weeks old consistently demonstrated MBP and PLP at levels 40% of normal, while those treated at 4 and 8 weeks old showed higher levels, albeit with high variability between animals[50]. Gray-Edwards et al.[40] found that AAV treatment only partially corrected pale LFB (Luxol Fast Blue) staining and myelin integrity loss evident on TEM in GM1 cats. A surprising result was that oligodendrocyte number was not abnormally low in affected untreated animals, but increased in cats treated with AAV, while ultrastructural oligodendrocyte pathology was partially corrected. This leads to an intriguing hypothesis that treated animals produce more oligodendrocytes to compensate for early pathology. Though more myelin-specific work is needed in future gene therapy studies, current evidence indicates that myelin deficits occur before the typical age of AAV treatment or that AAV is ineffective at treating the underlying cause of myelin deficits. One explanation may be that oligodendrocytes are poorly treated by most AAV serotypes[77].

While white matter-specific experiments are the most informative, insight into how gene therapy affects myelin pathology can be obtained through indirect methods. Baek et al. 2010[45] found that cerebroside and sulfatide levels in AAV-treated mice were not fully normalized, which implicates early involvement of myelin structural components. *In vivo* MRS measurements of GPC+PCh, an indicator of membrane turnover, were almost completely normalized in AAV-treated cats, which could indicate that refractory pathology does not involve the increased turnover of myelin sheaths[40,76]. Finally, the contribution of secondary demyelination can be indirectly measured through neuron density, which appears to be well-corrected by AAV treatment of SD mice[50,54]. These findings implicate an early myelin-specific pathological mechanism that is relatively independent of the loss of neurons and axons.

Table 1. Trends in pathological changes to oligodendrocytes, axons, and myelin in GM1 and GM2 gangliosidosis

	Myelin			Oligodendrocytes			Axons			
	Cerebrosides/ Sulfatides	*Sheath Integrity*	*Protein/mRNA markers*	*Storage*	*Number*	*Cell Injury*	*Degenerative Changes*	*Axon Number*	*Cell Body Number*	*Number Myelinated*
GM1										
Human		NC[41]↓[41]	↓[49]	NC[41,46,49]	↓[41,49]	↑[49]	NC[41,49]	↓[49]		↓[41,49]
Mouse	↓[43-45]	↓[43]								
Cat	↑[48]*	↓[40]		NC[40]	NC[40]	↑[40]				
Dog	↓[38]						↑[38]			↓[38]
GM2										
Human	↓[42,46,78]	↓[42]			NC[42]		↑[42]			↓[42]
Mouse	↓[46]		↓[50]				NC[52]↑[50]		↓[50,54]	
Cat	↓[23,46]	NC[37]					↑[37]	NC[37]		NC[37]
Sheep							↑[39]			
Dog		NC[51]		↑[51]			↑[51,53]		NC[51]	

*Measured cerebrosides/sulfatides in CSF rather than CNS parenchyma

↑: increased from normal, ↓: decreased from normal, NC: no change from normal

Table 2. Studies involving animal models treated with gene therapy

First Author	Year	Disease	Species	Route	Vector
Guidotti[64]	1999	GM2 (TSD)	Mouse	Intravenous, Intramuscular	Adenovirus
Takaura[65]	2003	GM1	Mouse	Intravenous	Adenovirus
Bourgoin[66]	2003	GM2 (SD)	Mouse	Intracranial (intracerebral)	Adenovirus
Kyrkanides[67]	2005	GM2 (SD)	Mouse	Intraperitoneal	Lentivirus
Cachon-Gonzalez[69]	2006	GM2 (SD)	Mouse	Intracranial (striatum)	AAV1
Kyrkanides[68]	2007	GM2 (SD)	Mouse	Intraperitoneal	Lentivirus
Broekman[44]	2007	GM1	Mouse	Intracranial (ICV)	AAV1
Broekman[79]	2009	GM1	Mouse	Intracranial (hippocampus)	AAV1
Baek[45]	2010	GM1	Mouse	Intracranial (thalamus, DCN)	AAV1
Sargeant[54]	2011	GM2 (SD)	Mouse	Intracranial (striatum)	AAV1
Cachon-Gonzalez[70]	2012	GM2 (SD)	Mouse	Intracranial (striatum, hippocampus, cerebellum)	AAV1
Bradbury[71]	2013	GM2 (SD)	Cat	Intracranial (thalamus)	AAV1 AAVrh8
Cachon-Gonzalez[50]	2014	GM2 (SD)	Mouse	Intracranial (striatum, cerebellum)	AAV1
McCurdy[72]	2014	GM1	Cat	Intracranial (thalamus, DCN)	AAVrh8 AAV1
McCurdy[22]	2015	GM2 (SD)	Cat	Intracranial (thalamus, DCN)	AAVrh8
Rockwell[23]	2015	GM2 (SD)	Cat	Intracranial (thalamus, ICV)	AAVrh8
Weismann[80]	2015	GM1	Mouse	Intravenous	AAV9
Walia[81]	2015	GM2 (SD)	Mouse	Intravenous	AAV9
Gray-Edwards[25]	2015	GM2 (SD)	Cat	Intracranial (thalamus, DCN, ICV)	AAV1 AAVrh8
Bradbury[21]	2015	GM2 (SD)	Cat	Intracranial (thalamus)	AAVrh8
Tropak[82]	2016	GM2 (SD)	Mouse	Intravenous	AAV9

Bradbury[24]	2017	GM2 (SD)	Cat	Intracranial (Thalamus, DCN, ICV)	AAV1 AAVrh8
Gray-Edwards[76]	2017	GM1	Cat	Intracranial (thalamus, DCN)	AAVrh8 AAV1
Gray-Edwards[48]	2017	GM1	Cat	Intracranial (thalamus, DCN)	AAVrh8
Gray-Edwards[73]	2018	GM2 (TSD)	Sheep	Intracranial (thalamus, ICV)	AAVrh8
Gray-Edwards[40]	2020	GM1	Cat	Intracranial (thalamus, ICV)	AAVrh8
Taghian[74]	2020	GM2 (TSD)	Sheep Human	Intrathecal (CM)	AAV9
Lahey[60]	2020	GM2 (SD)	Mouse	Intravenous	AAV9, PHP.B
McCurdy[83]	2021	GM2 (SD)	Cat	Intracranial (thalamus, DCN)	AAVrh8

SD: Sandhoff Disease, TSD: Tay-Sachs Disease, ICV: intracerebroventricular, DCN: deep cerebellar nuclei, CM: cisterna magna, AAV: adeno-associated virus

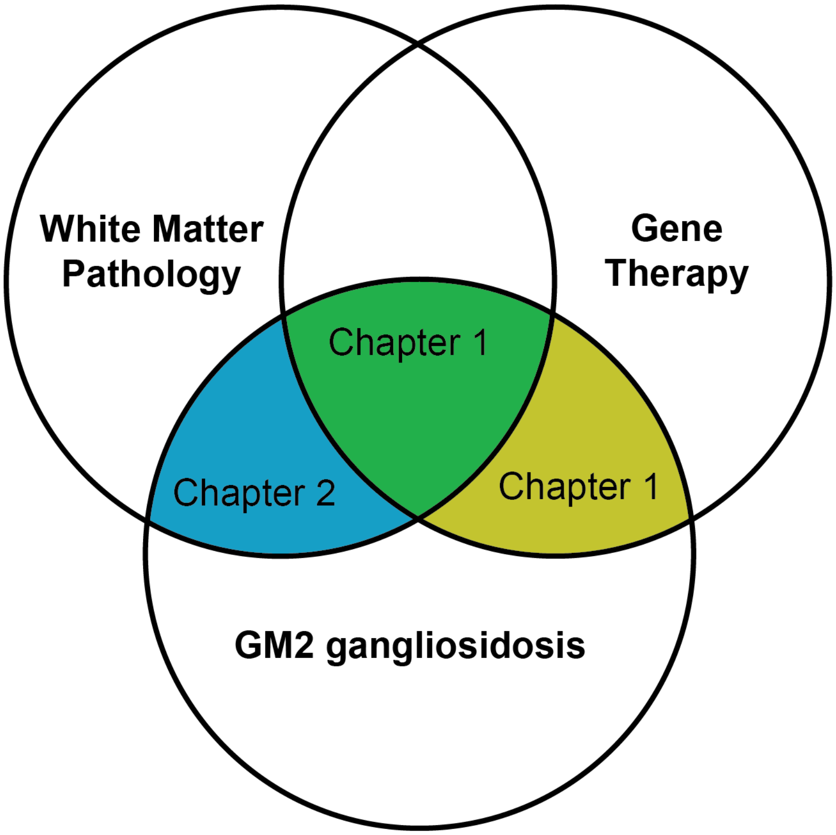

Figure 1. Scope of this dissertation. Filled areas are the focus of this dissertation.

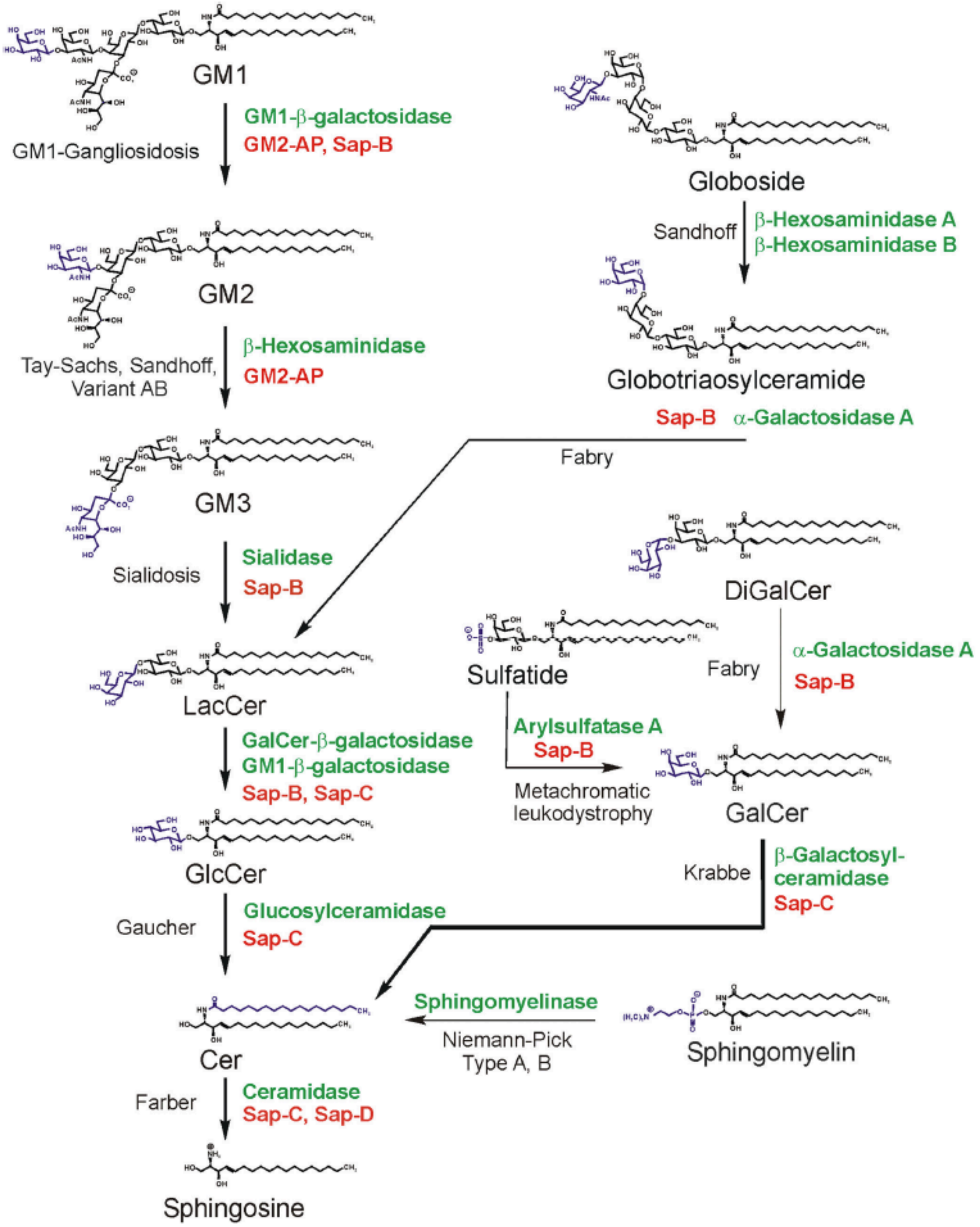

Figure 2. **Pathway of lysosomal sphingolipid degradation**. Activator proteins are indicated in red and hydrolases are represented in green, with the metabolic disease resulting from their dysfunction is in black to the left of the arrow. Variant AB: variant of GM2 gangliosidosis caused by deficiency of GM2 activator protein (GM2-AP), Sap: sphingolipid activator protein. Adapted from Sandhoff & Harzer, 2013[8]

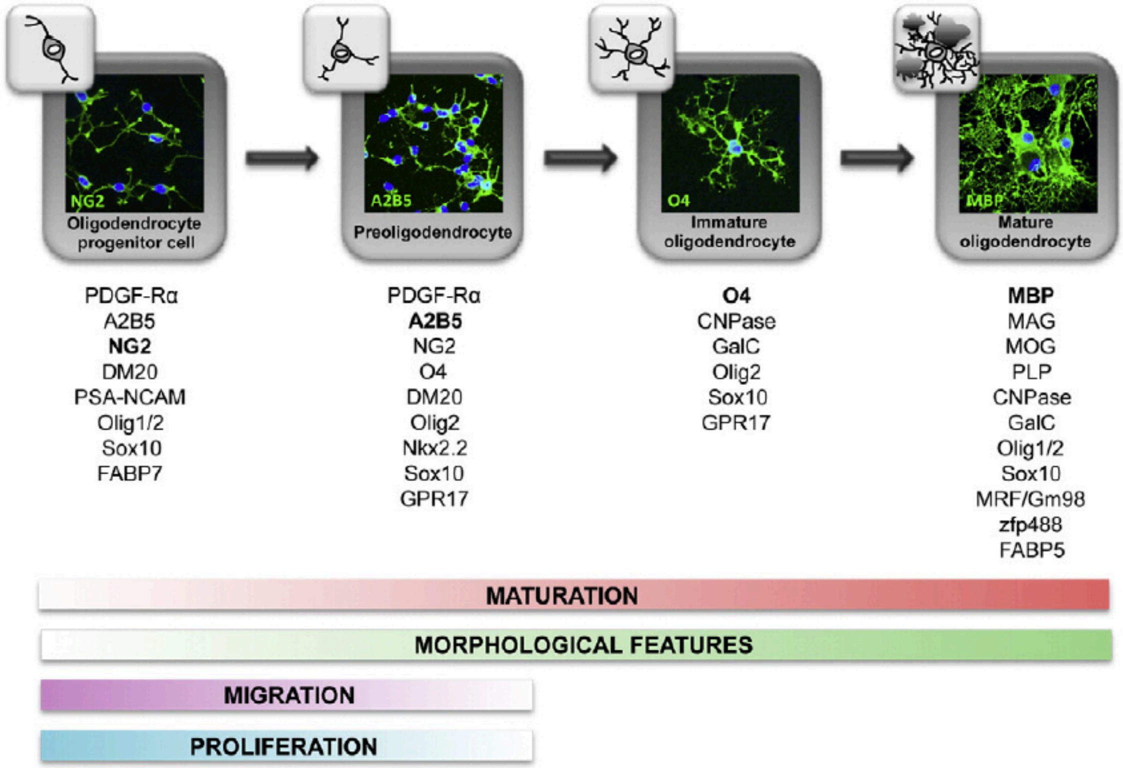

Figure 3. Markers of oligodendrocyte maturation. Stages of oligodendrocytes are differentiated from each other based on morphology, function, and expression of protein markers. CNPase: 2',3'-cyclic nucleotide 3'-phosphodiesterase, FABP: fatty-acid-binding proteins, GALC: galactocerebroside C, MAG: myelin associated glycoprotein, MBP: myelin basic protein, MOG: myelin oligodendrocyte glycoprotein, MRF: myelin gene regulator factor, PDGF-Rα: platelet-derived growth factor receptor, PLP: proteolipid protein, PSA-NCAM, polysialic acid-neural cell adhesion molecule; zfp, zinc finger proteins. Adapted from Barateiro & Fernandes, 2014[27]

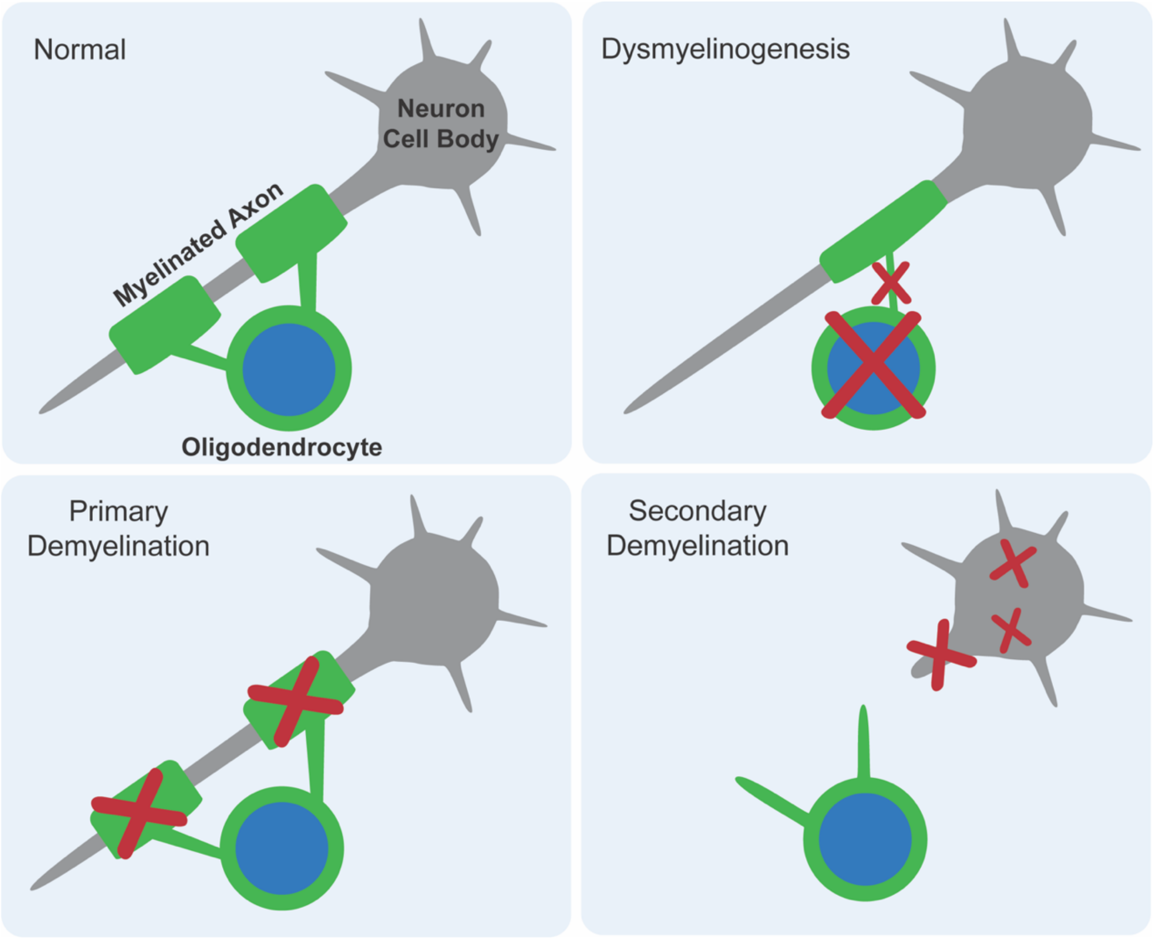

Figure 4. Proposed mechanisms for myelin deficits in the central nervous system. In normal tissue, each oligodendrocyte modifies its own cell membrane to myelinate one axon. If dysmyelinogenesis occurs, pathology within the oligodendrocyte, early myelin structures, or neuroaxonal communication leads to an abnormally myelinated axon. In primary demyelination, the oligodendrocyte is functional and myelin is formed properly, but then degraded. In secondary demyelination, neuroaxonal dysfunction leads to axonal loss, resulting in the overall loss of myelinated axons.

Chapter 1

Intravenous AAV gene therapy improves pre- and post-mortem outcomes in feline Sandhoff Disease

Anne S Maguire[1,2], Elise B Diffie[1,2], Amanda L Gross[1,2], Morgan Sturgeon[1,2], Jordan Doss[1,2], Hannah G Lahey[3,4], Nathan Linh Ta[5], Thomas N Seyfried[5], Heather Gray-Edwards[3,4], Miguel Sena-Esteves[3,4], Douglas R Martin[1,2]

[1]Scott-Ritchey Research Center, [2]Department of Anatomy, Physiology & Pharmacology, College of Veterinary Medicine, Auburn University, Auburn, Alabama, USA
[3]Department of Neurology, [4]Horae Gene Therapy Center, University of Massachusetts Medical School, Worcester, Massachusetts, USA
[5]Department of Biology, Boston College, Chestnut Hill, Massachusetts, USA

Introduction

Sandhoff Disease (SD) and Tay-Sachs Disease (TSD) are neurodegenerative lysosomal storage diseases that result in the death of affected children before 4 years of age. Because there are no FDA-approved therapies available, current treatment strategies are limited to palliation. SD and TSD are clinically similar forms of GM2 gangliosidosis (GM2), so their pathogenesis is directly tied to the absence of ß-hexosaminidase (Hex) and subsequent accumulation of GM2 ganglioside in neuronal lysosomes. This lesion results in a cascade of pathological effects throughout the body, but primarily in the central nervous system (CNS). A feline model of SD is a valuable intermediate step between mice and human clinical trials, and most faithfully recapitulates the infantile form of SD.

Though enzyme replacement, stem cell, and chaperone therapies have been thoroughly explored as treatment strategies for SD, none have achieved the level of success in prolonging animal model longevity as gene therapy. Through injection of adeno-associated viral (AAV) vectors containing the genes of interest, Hex activity and GM2 ganglioside storage deficits are consistently improved with a variety of capsids, delivery routes, and animal models. AAV1, AAV2 and AAVrh8 were used in early investigations, but recently AAV9 has emerged as the gold standard due to its ability to cross the blood-brain-barrier. Intracranial treatment has proven the most effective delivery route in SD cats so far, with injection into the thalamus/DCN (deep cerebellar nuclei) or thalamus/lateral ventricle quadrupling lifespan[22,23] (unpublished data). It is the lead delivery route in a clinical trial that began earlier this year (2021), the first to evaluate gene therapy in GM2 (ClinicalTrials.gov Identifier NCT04669535).

Concerns about the safety of intracranial surgery in young children with neurological disease has led to the investigation of less invasive routes. Intrathecal delivery using a specialized technique of reaching the cisterna magna through lumbar puncture was developed in TSD sheep and translated to the treatment of 2 children in an expanded access clinical trial[74]. Intravenous (IV) delivery is even less invasive, effective in SD mice[50] and cats with the closely related LSD GM1 gangliosidosis (GM1) (publication under review), and was the lead route in an ongoing clinical trial for GM1 (NCT03952637). However, simultaneous delivery of vectors expressing the α and ß subunits to a given cell is more difficult in intrathecal and intravenous deliveries and is required for efficient assembly of Hex in the endoplasmic reticulum. Recently, Lahey et al.[60] designed a bicistronic AAV vector in which each virus particle encodes both subunits, and demonstrated its efficacy in SD mice. Therefore, the primary purpose of this study is to evaluate the efficacy of an IV-delivered, bicistronic, AAV vector in SD cats.

The secondary objective of this study is to include a detailed examination of this treatment method on the populations of distinct cell types within the brain using novel whole-slide image analysis techniques. Neurons are directly affected by GM2 storage deficits; oligodendrocyte pathology is directly tied to CNS myelination, while microglia and astrocytes are indicators of neuroinflammation. Neuronal cell death is known to occur in specific regions of SD mice and be partially corrected by AAV treatment[50,54]. Oligodendrocyte number is decreased on qualitative assessments of GM1 human patients[49], but unchanged from normal levels upon quantitative analysis throughout the CNS of GM1 cats[40]. Data on oligodendrocyte numbers in GM2 have yet to be published. SD cats exhibit activated microglia, while GM1 cats displayed increased numbers of astrocytes and microglia. These phenotypes were partially normalized with AAV gene therapy[24,40]. As performed in Gray-Edwards et al.[40], whole-slide cell quantification is an increasingly popular method for addressing questions about cell populations. It has been shown to be powerful and customizable, able to meet the needs of specific needs of each experiment[84]. This study adds to the scarce knowledge of CNS cell populations in SD cats through the open-source digital pathology software QuPath[85] applied to whole slides with established immunohistochemistry stains (IHC).

Methods

AAV Vector Preparation

Preparation of the AAV9 bicistronic vector was performed similarly to previously published methods of AAV9-Bic in mice[60], except that feline HEXA and HEXB cDNAs were used in this study. The vector includes a centrally located, bidirectional enhancer/promoter complex consisting of a cytomegalovirus (CMV) enhancer flanked by 2 chicken β-actin promoters in opposite directions, with no introns. The low and high doses were 5E13 vector genomes/kg and 2E14 vector genomes/kg, respectively.

Animals and AAV Treatment

A breeding colony of SD cats is maintained at Scott-Ritchey Research Center at Auburn University, and all experiments in this study were approved by its Institutional Animal Care and Use Committee. Affected SD cats were treated between 0.77 and 1.47 months of age (mean 1.10±0.15) and 0.38 and 0.70 kg (mean 0.49±0.15). An intravenous catheter was placed in the cephalic vein and flushed with saline. Vector was delivered slowly over a period of 1-2 minutes via the catheter, which was subsequently flushed with saline. Cats were monitored for at least 3 hours post-treatment for any adverse reactions. Euthanasia was performed with cardiac injection of pentobarbital and animals were subsequently perfused with saline. AAV-treated cats were euthanized 16 weeks post treatment (low dose n=4, high dose n=3) or followed until they reached the predetermined humane endpoint of inability to stand on 2 consecutive days (low dose n=4, high dose n=4). Controls were age-matched untreated normal cats ($n \geq 3$) and untreated SD cats at the same predetermined humane endpoint ($n \geq 3$).

Tissue Preparation

Brains were divided into 9 transverse blocks of 0.6 cm from the frontal pole through the cerebellum (Figure 5). Blocks from the right hemisphere were frozen in optimal cutting temperature (OCT) medium and used for measuring specific enzyme activity by synthetic fluorogenic substrates based on 4-methylumbelliferone (4MU). Blocks from the left hemisphere were halved to 0.3

cm and either flash frozen in liquid nitrogen or fixed in 10% formalin. Frozen tissue was stored at -80°C and used for high-performance thin layer chromatography (HPTLC) assays to quantify storage material. Formalin-fixed tissue was embedded in paraffin blocks and used for LFB (Luxol Fast Blue) or IHC staining.

MRI and MRS

Cats were placed under general anesthesia with dexmedetomidine and ketamine and maintained with isoflurane. MRI and MRS data were collected as previously described[40,48] on a 7 Tesla scanner (Siemens Healthcare) on SD cats immediately before necropsy (n=3 for untreated, n=15 for all treated cats) and on normal cats at 4-5 months, 8 months, and 12 months of age (n=3 per time point). To acquire MRS data, voxels were placed in the thalamus (7 x 6 x 8 mm), parietal cortex (7 x 6 x 8 mm), and cerebellum (7 x 7 x 8 mm). MRS data were processed with LC model and internal water scaling (http://www.s-provencher.com/lcmodel.shtml).

Cerebrospinal Fluid (CSF) Analysis

Cats were placed under general anesthesia as described earlier for MRI and MRS acquisition. CSF was collected from the cisterna magna and immediately frozen at -80°C. A Cobas C311 chemistry analyzer (Roche Hitachi) was used to measure ALT (alanine aminotransferase) and LDH (lactate dehydrogenase). Acquisition of Hex specific activity is described below.

Enzyme Activity Assays

Several frozen sections were cut from the OCT-frozen blocks and homogenized manually in 50 mM citrate phosphate buffer (pH 4.4) as previously described[72]. The activity of HexA, Total Hex, Bgal, and Mann enzymes were measured with synthetic fluorogenic substrate 4MU as previously described[72], except 10μL was used for Bgal and Mann, 5μL for Total Hex, and 20μL for HexA. Specific activity was normalized to protein concentration through the Lowry method, then expressed as nmol 4MU/mg/hour.

Lipid extraction and ganglioside quantification

Punch biopsies 8mm in diameter were taken from frozen CNS sections and lyophilized overnight. The HPTLC protocol was performed as previously described[23].

Luxol Fast Blue Staining

Slides underwent a rehydration series of 8 minutes in Hemo-D (Scientific Safety Solvents, Keller, TX, USA) or xylene (3x), 2 minutes in 100% ethanol (2x), 2 minutes in 95% ethanol (2x), 2 minutes in distilled water, then incubated overnight at room temperature in LFB solution (0.1% in 95% alcohol with acetic acid, Electron Microscopy Sciences, Hatfield, PA, USA). In groups of 3 or 4 with at least one normal sample, slides were dipped in lithium carbonate (0.05%, Diagnostic BioSystems, Pleasanton, CA, USA) and 70% ethanol until the gray matter was clear. After a rinse in distilled water, slides were counterstained with Mayer’s Hematoxylin (Electron Microscopy Sciences) for 3 minutes, followed by a 3-minute rinse in running water. Slides dried overnight at room temperature and were coverslipped the following day.

Immunohistochemistry

Slides were dehydrated in the same series as for LFB staining, then underwent antigen retrieval with Antigen Decloaker (Biocare Medical, Concord, CA, USA) in a decloaking chamber (Biocare Medical). After rinsing in distilled water, slides were loaded into an IntelliPath FLX slide stainer (Biocare Medical). The following protocol was applied to all stains, with exceptions noted below. All reagents were manufactured by Biocare Medical unless otherwise noted:

- General protocol:
    1. Block: IP FLX Peroxidase, 5 minutes
    2. Block: IP FLX Background Punisher, 5 minutes
    3. Primary antibody: Diluted in Da Vinci Green Diluent
    4. Secondary antibody: MACH 2 Rabbit HRP-Polymer, 30 minutes
    5. Chromogen: Betazoid DAB, 5 minutes
    6. Counter-stain: Tacha’s Auto Hematoxylin, 3 minutes
- Buffer wash throughout: TBS Auto Wash Buffer
- GFAP primary antibody: 1:200 dilution, 20 minutes
- Iba-1 primary antibody: 1:750 dilution, 30 minutes

- NeuN primary antibody: Abcam (Cambridge, MA, USA), 1:200 dilution, 60 minutes
- Calbindin
    - Primary antibody: Sigma-Aldrich (St Louis, MO, USA), 30 minutes
    - Secondary antibody: MACH 2 Mouse HRP-Polymer, 30 minutes
- Olig2 primary antibody: Abcam, 1:200 dilution, 30 minutes

Slides dried overnight at room temperature and were coverslipped the following day.

Image Acquisition of Stained Slides

A Keyence BZ-X810 (Keyence, Itasca, Illinois, USA) was used to acquire all images. After brightness correction and scout scans at 4x, relevant regions were outlined at 20x and individual images were acquired. Images were stitched together with the built-in software and saved in the Big TIFF format. Files were imported into QuPath software[85] version 0.2.3 where they were qualitatively assessed, with representative images exported for inclusion in figures.

Quantification of Stained Slides

After images were acquired and imported into the QuPath software (described above), algorithms were designed for each stain and tested on 2-3 images from cats in different treatment groups. For the nuclear stains (Olig2 and NeuN), algorithms were designed to count the number of stained nuclei per mm^2 by using the cell detection function based on optical density, then applying an object classification to detected cells to differentiate DAB-positive cells from hematoxylin-positive cells if necessary. For the cytoplasmic IHC stains (GFAP, Iba-1, calbindin) and LFB, algorithms were simple thresholders to calculate the percentage of stained pixels. For the NeuN-stained slides, two different algorithms were used because the hematoxylin was a substantially different shade between two batches of slides. In addition, NeuN does not stain Purkinje cells within the cerebellar cortex, so both calbindin (which only stains Purkinje cells) and NeuN were used to quantify neurons in that region. Due to the high density of neurons within the granular layer of the cerebellum, differentiation of individual nuclei was impractical, and the NeuN quantification metric was switched from cells/mm^2 to percentage of stained pixels. Algorithm specifications are detailed below.

The first step in the analysis of each image was to manually input the magnification as 20x and pixel length as 0.2 x 0.2 µm, since that information was not imported automatically with the metadata attached to each slide. Second, a stain vector was applied, if needed, to optimize the software’s differentiation between hematoxylin and DAB or LFB (stain vectors provided below). Third, regions of interest (parietal cortex white matter/gray matter, thalamus, cerebellar cortex white matter/gray matter, DCN, brainstem) were hand-drawn using the brush and wand tools. For LFB-stained slides, determination of white/gray matter boundaries during this step was performed while viewing the hematoxylin-only “channel” to avoid bias introduced by LFB staining. Fourth, the algorithm was applied and the resulting data manually recorded in a Microsoft Excel file.

Algorithms

- Olig2
    - Stain vectors:
        - Hematoxylin: 0.739 0.538 0.405
        - DAB: 0.452 0.589 0.67
        - Background: 240 240 240
    - Cell detection:
        - Detection image: Optical density sum
        - Requested pixel size: 0.2 μm
        - Background radius: 10 μm
        - Median filter radius: 0 μm
        - Sigma: 1.0 μm
        - Minimum area: 6 μm^2
        - Maximum area: 400 μm^2
        - Threshold: 0.25
        - Maximum background intensity: 2.0
        - Split by shape: true
        - Exclude DAB: false
        - Cell expansion parameters: 0 μm
        - Include cell nucleus: true
        - Smooth boundaries: true
        - Make measurements: true
    - Object classification

    - Channel filter: DAB
    - Measurement: DAB OD Mean
    - Threshold: 0.08
    - Above: Positive
    - Below: Negative
- NeuN
  - Stain vector (faint hematoxylin)
    - Hematoxylin: 0.50236 0.60145 0.6212
    - DAB: 0.31918 0.51223 0.79734
    - Background: 223 223 220
  - Stain vector (strong hematoxylin)
    - Hematoxylin: 0.607 0.628 0.488
    - DAB: 0.401 0.573 0.715
    - Background: 221 223 221
  - Cell detection (faint hematoxylin)
    - Detection image: Optical density sum
    - Requested pixel size: 0.2 μm
    - Background radius: 18 μm
    - Median filter radius: 0 μm
    - Sigma: 1.5 μm
    - Minimum area: 6 μm^2
    - Maximum area: 600 μm^2
    - Threshold: 0.3

        - Maximum background intensity: 2.0
        - Split by shape: false
        - Exclude DAB: false
        - Cell expansion parameters: 3 μm
        - Include cell nucleus: true
        - Smooth boundaries: true
        - Make measurements: true
    - Cell detection (strong hematoxylin)
        - Same as faint hematoxylin except threshold = 0.4
    - Object classification (faint hematoxylin) #1
        - Object filter: Detections (all)
        - Channel filter: Hematoxylin
        - Measurement: Nucleus Hematoxylin OD Mean
        - Above: Negative
        - Below: Positive
    - Object classification (faint hematoxylin) #2
        - Object filter: Detections (all)
        - Channel filter: DAB
        - Measurement: Nucleus DAB OD Max
        - Above: Positive
        - Below: Negative
    - Object classification (strong hematoxylin)
        - Object filter: Detections (all)

        - Channel filter: DAB
        - Measurement: Nucleus DAB OD Mean
        - Threshold: 0.15
        - Above: Positive
        - Below: Negative
    - Stain vector (for strong-hematoxylin slides, cerebellar cortex only)
        - Hematoxylin: 0.72 0.641 0.265
        - DAB: 0.435 0.568 0.699
        - Background: 217 220 220
    - Thresholder (for strong-hematoxylin slides, cerebellar cortex only)
        - Resolution: Very high
        - Channel: DAB
        - Prefilter: Gaussian
        - Smoothing sigma: 0
        - Threshold: 0.20
        - Above threshold: Positive
        - Below threshold: Negative
        - Region: Any annotations
- Calbindin
    - Stain vector: Default
    - Thresholder: same as NeuN thresholder, except Threshold = 0.30
- GFAP
    - Stain vector: Default

        - Thresholder: same as NeuN thresholder
- Iba-1
    - Stain vector: Default
    - Thresholder: same as NeuN thresholder, except Threshold = 0.15
- LFB
    - Stain vector
        - Hematoxylin: 0.644 0.722 0.251
        - LFB: 0.777 0.516 0.359
        - Background: 238 238 236
    - Thresholder:
        - Channel: LFB
        - Above threshold: Positive
        - Below threshold: Negative

Data Analysis and Statistics

All statistical analyses and graphs were generated with GraphPad Prism version 9.1.2 for Mac OSX (GraphPad Software, La Jolla California USA, www.graphpad.com). All tests were Welch's ANOVAs with alpha values of 0.05 and Dunnett's T3 multiple comparisons test for post-hoc analyses. For weight, post-hoc tests included every pairwise comparison. For all other analyses, post-hoc tests included untreated SD group versus normal 4-5 month old and every AAV-treated group, each AAV-treated group versus its age-matched normal group, and every pairwise comparison of AAV-treated low dose short-term, low dose long-term, high dose short-term, and high dose long-term.

Results

The low dose of AAV approximately doubled the lifespan of SD cats, while the high dose tripled it (untreated: 4.2±0.32, low dose: 8.3±1.23, high dose: 12.4±2.74 months). The longest-lived cat (11-1355) was 16.0 months at humane endpoint (Figure 1A). AAV treatment improved the quality of life in SD cats as measured by weight (Figure 1B) and a neurological clinical rating score (Figure 1C) in a dose-dependent fashion, though even the high dose failed to normalize both metrics. By far the most dramatic clinical improvement observed was the reduction of tremors, the most debilitating feature of feline SD. While untreated SD cats quickly develop overt full-body tremors that interfere with their ability to stand, most AAV-treated cats displayed fine resting tremors, if any, that stabilized early in disease progression. Fine tremors progressed to full-body tremors by the humane endpoint in 3 of 4 cats treated with the low dose but none of the cats treated with the high dose (Table 1). Treated animals typically reached the predetermined humane endpoint through severe limb paresis or paralysis (Table 1) due to spinal cord compression (Figure 2).

T2-weighted MR images acquired with a 7T scanner demonstrate that AAV treatment partially restores gray/white matter distinction and minimizes brain atrophy (Figure 3A). MRS data show that the cerebellum is more impacted in untreated SD than the parietal cortex and thalamus, with significant increases in both NAA+NA-Hex (N-acetylaspartate + N-acetylhexosamine) and GPC+PCh (glycerophosphocholine + phosphocholine) (Figure 3B). NAA+NA-Hex, which in GM2 gangliosidosis is a merging of the peaks indicating NAA and storage material (N-acetylhexosamine), is also significantly increased in the parietal cortex and thalamus of untreated SD cats (Figure 3B). GPC+PCh, an indicator of membrane turnover, is unchanged from normal in the parietal cortex and thalamus of untreated SD cats (Figure 3B). Myoinositol (Ins), thought to be an indicator of neuroinflammation, remains unchanged in all 3 regions (Figure 3B). AAV treatment at both doses normalizes NAA+NA-Hex in all 3 regions, and the high dose of AAV reduces the abnormally high GPC+PCh levels in the cerebellum (Figure 3B).

CSF levels of aspartate aminotransferase (AST) and lactate dehydrogenase (LDH), indicators of cell damage within the CNS, are significantly increased in untreated SD cats at humane endpoint (4-5 months of age) (Figure 4A, B). AAV-treated SD cats have less AST and LDH at 5 months of age than untreated SD cats, with the high dose being more effective at reducing these levels (Figure 4A, B). Specific activity of all isozymes of Hex (Total Hex) is decreased to 6.85% of normal in untreated SD cats and restored to near-normal or above-normal levels in cats treated with both doses across ages (Figure 4C).

Specific activities of both HexA and Total Hex follow similar patterns when compared to age-matched normal controls (Figure 5). Activity levels in untreated SD cats were 10% of normal or less across all CNS sections, with the exception of section N at 17%. In the cerebral cortex and thalamus (sections A-F), activity levels for AAV-treated cats were similarly low (<15% of normal), with the exception of one high-dose treated cat (11-1416) whose levels ranged from 17% to 80%. More of a dose-dependent response to treatment was seen in the cerebellum and brainstem regions, with the high dose long-term group having significantly higher levels of Hex than untreated SD. The spinal cord (J-P) was especially responsive to the high dose, with most cats ranging from 25% to 100% of normal Hex levels. The opposite pattern was seen in the activity levels of similar lysosomal enzymes ß-galactosidase (Bgal) and α-mannosidase (Mann), in which cats with low levels of Hex activity had high levels of Bgal and Mann activity, and vice versa.

Storage products (GM2 ganglioside and total sialic acid) were significantly increased in untreated SD cats, reduced 16 weeks after AAV treatment, then increased in the longer-lived cats (Figure 6). Total sialic acid storage products were statistically elevated to 1.8-4.2 times normal in most regions of the CNS, including parietal cortex, thalamus, occipital cortex, cerebellum, and cervical intumescence of the spinal cord. GM2 ganglioside was below detection levels in all normal tissues, as expected. Both total storage and GM2 ganglioside levels in AAV-treated short-term cats were partially normalized in all regions, with total storage levels in the cerebellum and brainstem at or below normal levels. Long-term treated cats had total storage and GM2 ganglioside levels at or above untreated SD levels in most regions.

The strongest trend in the neuroinflammatory data was that long-term treated cats have higher levels of both GFAP (glial fibrillary acidic protein) and

Iba-1 (ionized calcium-binding adaptor molecule 1) staining than their short-term counterparts (Figure 7). Consistent trends were observed in the quantification of both GFAP and Iba-1, especially when considered in tandem, but statistical significance was rarely achieved due to the artifactually high variability introduced by intermittent regions of high background staining. In most brain regions examined, untreated SD cats had higher than normal levels of these markers, with the most severely affected region being the cerebellar cortex, though GFAP in the parietal cortex was the highest overall. In general, AAV-treated cats euthanized 16 weeks post-treatment had values at or below untreated SD levels. Cats in the long-term cohorts had higher levels of both GFAP and Iba-1 than their short-term counterparts in the parietal cortex, thalamus, and cerebellar cortex, with values well above normal and untreated SD cats. The DCN and brainstem regions were an exception, with minimal differences between the long-term and short-term AAV groups of either dose. Upon qualitative evaluation, the activated morphology of astrocytes and microglia was more prevalent in untreated SD and long-term AAV-treated cats.

Mild neuronal loss was inconsistently observed in SD cats, with the number of NeuN positive cells at 75-80% of normal in the parietal cortex and thalamus, 30% of normal in the DCN, and around normal levels in the cerebellar cortex and brainstem (Figure 8). In general, the short-term cats (16 weeks post-treatment) had increased neuronal count, often achieving near-normal levels, especially with the high dose. Longer-lived cats had fewer neurons than their short-term counterparts, often dropping below the levels seen for untreated SD cats. A notable exception to these patterns occurred in the DCN and brainstem, in which these patterns were mostly reversed (low dose cats had more NeuN positive cells than high dose cats, high dose long-term cats had more neurons than their short-term counterparts). High variability preventing statistical significance was observed with neuronal quantification, likely due to uneven IHC staining.

The number of oligodendrocytes labeled by Olig2 was reduced to around 50% normal in the parietal cortex, thalamus, and cerebellar cortex, and around 75% in the DCN and brainstem (Figure 9). In the parietal cortex and thalamus, AAV treatment partially normalized oligodendrocyte levels in a dose-dependent fashion. In the cerebellar cortex, DCN, and brainstem, oligodendrocyte numbers were closer to normal with both dose groups, with long-term cats having above-normal levels of oligodendrocytes in the brainstem. The high variance of the LFB staining makes it difficult to draw concrete conclusions, but in general the most affected areas in untreated SD cats are the parietal cortex, thalamus, and cerebellar cortex, with dose-dependent partial normalization. LFB staining in the DCN and brainstem was at approximately normal levels across untreated and all AAV-treated cats.

Discussion

The IV-delivered bicistronic AAV vector was effective at improving lifespan and quality of life in SD cats. Longevity almost doubled with the low dose and tripled with the high dose, and AAV-treated cats maintained a higher weight and

CRS than their untreated counterparts. Though promising, this improvement was not as substantial as the same vector/route combination in SD mice or intracranial delivery of monocistronic vectors in SD cats, which both approximately quadrupled lifespan[22,23,60]. Similar to previous AAV treatment of SD cats, by far the most dramatic clinical improvement was the reduction of severe tremors, presumed to be primarily cerebellar in origin. Overt tremors only developed in 3 of 15 AAV-treated cats (all at the low dose), with the age of onset delayed by 5 months compared to untreated SD cats.

Because severe tremors did not often lead to the humane endpoint of AAV-treated SD cats, long-term disease phenotypes had a chance to emerge. The most severe of these was spinal cord compression, evident upon necropsy of most AAV-treated cats. Clinically, these cats often displayed pelvic limb paresis or paralysis that led to the predetermined humane endpoint (unable to stand on 2 consecutive days). Bony abnormalities have been recorded in radiographs and 3T MR images in the cervical spine and coxofemoral regions in SD cats, though the pathogenesis of these changes is unknown[25]. These clinical signs are also observed in human patients with mucopolysaccharidosis (MPS), a family of LSDs that primarily affects connective tissue[86]. In AAV-treated cats, the more severe phenotype that develops with increased lifespan leads to the opportunity to investigate this pathology in more detail. In future studies, advanced spinal cord imaging (MRI or computed tomography), measurement of Hex specific activity in the intervertebral discs (IVD), and histologic evaluation of spinal cord tissue would all serve to elucidate the cause of these bony changes in SD cats.

MR images reveal partial normalization of atrophy and gray/white matter distinction with AAV treatment. In T2-weighted images of normal cats, white matter is hypointense to (darker than) gray matter because of the differential lipid content; white matter is lipid-rich due to its high proportion of myelin content. In SD cats, myelin loss causes an increase in white matter signal intensity, while lipid-rich storage products in the gray matter decrease its signal intensity. Therefore, MR images of untreated SD cats often show a lack of distinction between gray and white matter, as the lipid differential between them is reduced. In addition, the very hyperintense CSF signal just under the meninges becomes thicker in SD cats, as the brain parenchyma atrophies and CSF fills the resulting space. Images of AAV-treated cats show partial restoration of the gray/white matter distinction and a thinner line of CSF due to the reduction in atrophy. These results are similar to those of AAV-treated cats with GM1 through the intracranial route[40]. Though qualitative evaluation of signal intensities in 7T MR images is informative, quantification would add robustness to this valuable *in vivo* biomarker and should be investigated.

Metabolite levels measured by MRS indicated that some *in vivo* biomarkers of SD respond to AAV treatment. As a marker of neuronal health, NAA (N-acetyl aspartate) levels are abnormally low in GM1 cats[40] and other CNS diseases such as multiple sclerosis[87] and intra-cerebral hemorrhage[88]. However, in SD, the NAA metabolite peak overlaps with that of the storage products, obscuring the pure NAA peak. The cerebellum of untreated SD cats has the highest NAA+NA-Hex (N-acetyl-aspartate + N-acetyl-hexosamine) levels at 1.75x normal, though the parietal cortex and thalamus also have significantly higher levels. GPC+PCh (glycerophosphocholine + phosphocholine), an indicator of membrane turnover, is a reliable marker of pathology in GM1 cats[40] and appears to translate well to SD cats. Though it is logical that an indicator of membrane turnover would correlate with myelin pathology, more evidence would be needed to establish that correlation. Myoinositol (Ins) is used as a marker of inflammation in cats with GM1[40], but is unchanged from normal in SD cats. Any metabolite that was significantly different from normal in untreated SD cats was normalized in AAV-treated cats.

CSF analysis provides another medium for *in vivo* assessment of SD pathology and AAV treatment efficacy. AST and LDH are ubiquitously expressed enzymes that are released from cells following plasma membrane damage. High levels in the CNS are well-documented in a variety of neurological diseases including human TSD[89,90], canine GM1[91], and human meningitis[92]. Similar to intracranial AAV treatment in SD[21] and GM1[76] cats, IV treatment of SD cats in this study resulted in normalization of AST and LDH. Also measurable in the CSF was Hex specific activity, which is minimal in untreated SD cats. Hex activity was increased to normal levels in both doses of AAV-treated cats. The presence of Hex activity in the CSF could be considered counterintuitive, since CSF typically has very low cell counts. This could be due to the well-documented cross-correction phenomenon in which lysosomal enzymes leak from neurons.

Improvement in Hex activity was greatest in the spinal cord, with most cats achieving therapeutic levels of 20% of normal, and some regions close to normal. This is consistent with results from GM1 and SD mice treated intravenously with AAV9, including with the same bicistronic vector as this study[60,80]. Indeed, the spinal cord appears to be the best-transduced area with intravenous delivery of AAV, with mixed results in the brainstem, cerebellum, and cerebral cortex[60,80]. While the methods of this study did not distinguish the brainstem from the caudal portions of the cerebral brainstem and the entire cerebellum, in general the regions with the best Hex activity were found in the caudal region of the brain (cerebellum/brainstem) and the spinal cord. The specific activity of HexA and Total Hex is increased in AAV-treated cats and inversely correlated with ganglioside storage and the activity of compensatory hydrolases (Bgal and Mann).

Hex activity in cats treated with the high dose was most likely to achieve effective therapeutic levels (15-20% of normal) in the most effectively transduced CNS regions. Intravenous delivery did not result in the same levels of Hex that intracranial treatment achieved in SD cats, in which all brain regions had above-normal levels of activity[22,23], but more faithfully recapitulates the Hex activity seen in SD mice with IV delivery of this bicistronic vector[60]. In untreated SD, there are two easily measurable lysosomal effects of a reduction in Hex activity: storage products accumulate and the activity of other lysosomal hydrolases increases in an attempted compensatory mechanism. It is important to confirm that any increases in Hex activity coincide with reduction in ganglioside storage and Bgal and Mann activity. In AAV-treated cats, the high dose was more effective at improving Hex activity than the low dose, with corresponding decreases in storage, Bgal activity, and Mann activity. Of note is the fact that the cats in the high dose group often had lower levels of storage than cats in the low dose group, despite the fact that they lived 4 months longer on average. Taken together, these data demonstrate that IV delivery of this bicistronic vector translates well from SD mice to cats.

Whole-slide image analysis to quantify myelin and cell populations was successful to identify general patterns, even though variability was often too high to achieve statistical significance. Though similar to the one employed by Gray-Edwards et al. with GM1 cats[40], this method demonstrated that the open-source software QuPath is a viable alternative to the proprietary software Visiopharm. Preanalytical errors included differing regions between blocks and uneven staining. Though every effort is made to ensure the transverse slices at necropsy occur in the same place in every cat, differing brain sizes due to age and differential distribution of storage makes consistency difficult. During quantification, regions with varying white matter to gray matter ratios were more prone to variability for stains such as Olig2, due to the fact that many more oligodendrocytes are present in white matter than gray matter. The DCN (deep cerebellar nuclei) was particularly prone to variability in quantification because of its small size and drastic changes in gray/white matter ratio throughout the rostral-caudal plane. Though the Biocare slide stainer is the best option for achieving IHC staining in bulk and consistency between batches, its lack of agitation mechanism may have led to uneven staining in some slides. Cytoplasmic stains (GFAP, Iba-1, Calbindin) in particular are more prone to variability due to uneven staining, since simple thresholding algorithms do not subtract background staining as efficiently as cell identification algorithms. This could be improved in future studies by applying machine and deep learning algorithms that are rapidly becoming more accessible to biomedical researchers. Though LFB was chosen for this study to be consistent with qualitative observations of myelin in previous studies[40,49], more consistent quantification in the future would likely be achieved with antibodies to proteins specific to mature myelin such as MBP and PLP1.

Activation of astrocytes and microglia, hallmarks of neuroinflammation, was mitigated 16 weeks after AAV treatment but not in longer-lived cats. GFAP-positive staining was increased in untreated SD cats and long-term AAV-treated cats, coupled with the activated astrocyte morphology of thickened cellular processes[93]. Microglia followed a similar pattern, with increases in quantity and activated morphology (ameboid, with large cell bodies and short, thick processes), in untreated SD and long-term AAV treated cats. These results are consistent with previously published studies in SD[24] and GM1[40] cats, in which the increases of Iba-1 and GFAP staining, respectively, in untreated cats were reduced by intracranial AAV injection. It is likely AAV treatment is effective at reducing neuroinflammation, which then continues to accumulate in cats that live longer. Of note is the fact that in most regions, cats in the high dose group still had lower levels of staining despite the fact that they lived 4 months longer on average, supporting the hypothesis of dose-dependent efficacy.

The pattern of neuronal staining was the inverse of the pattern of neuroinflammation, likely due to neuronal loss. Although causation between neuroinflammation and neuronal loss is yet to be definitively established, both pathologies are consistent with a generalized neurodegenerative pattern. In CNS diseases such as Parkinson's Disease[94], Alzheimer's Disease, and prion diseases[95], neuroinflammation precedes neuronal loss, so an interesting area of future studies could be to investigate the timing of the pathology of these cell populations over the course of untreated SD progression. Of note is that the calbindin-positive Purkinje neuron presence mirrors that of the NeuN-positive non-Purkinje neuronal population in the cerebellar cortex, implying that these cells crucial to relaying information throughout and from the cerebellum are affected by SD and AAV-treatment in a similar fashion. More informative than simple neuronal population counts would be a detailed evaluation of specific functional regions of neurons, as previously performed in SD mice[50,54]. Gross neuronal loss was not evident in SD mice except for the VPM/VPL nuclei of the thalamus[54], where intracranial AAV treatment was successful in restoring neuronal cell count[50]. Though this precise regional localization of neuronal populations would be more difficult in the more heterogeneous feline brains, it would provide a valuable focus on the effects of disease and treatment on neuronal function, and possibly correlate with clinical signs.

Oligodendrocyte number and myelin are below normal levels in most regions measured, with partial normalization through AAV treatment. In untreated GM1 cats, a reduction in Olig2-positive cell numbers was not observed in the 6 regions examined (striatum, thalamus, parietal cortex, temporal lobe, occipital cortex, and cerebellum)[40], in contrast to the current study in which it was observed in all regions. A biological explanation for this difference in myelin pathology between two otherwise very similar pathological processes is not obvious, though perhaps differences in methodology or severity of clinical disease could be the cause. One similar pattern between both studies is the increase in oligodendrocyte number in some regions to above-normal levels post-treatment. This could be attributed to pathology within existing oligodendrocytes being compensated for post-treatment by differentiation of OPCs into new mature oligodendrocytes. Myelin loss, as determined by a decrease in LFB staining, matched GM1 cats in that there was extreme loss in the parietal cortex and cerebellum and less severe loss in the thalamus. The DCN and brainstem, in which little to no myelin loss was observed in SD cats, were not evaluated in the GM1 cats.

Mild pathology in the brainstem of untreated SD cats is not limited to mild decreases in myelin and oligodendrocyte number, as neuroinflammation and neuronal loss are least severe in the brainstem as well. In addition, AAV treatment may have a more dramatic effect in the brainstem than other regions, since neuroinflammation does not appear to increase in long-term treated cats, and oligodendrocytes increase to above-normal levels. When considered with the

Hex activity and storage data, the brainstem appears to be the best-treated region in the brain, though this could be due partly to milder disease in the brainstem at the outset.

Though differences between the low and high dose are detected in most metrics examined in this study, there is the possibility that the differences detected are not strictly due to dose. The titering process for AAV vector is often considered imprecise by experts within the field, with results from the same batch being several-fold different from each other when measured on different days (unpublished data). New methods are currently being developed for titering virus, such as measurements based on charge/weight and counting of virus particles on TEM. For this study, since the difference between the high dose and low dose is only four-fold, it is possible that there is more overlap between the doses than is currently measurable. Consistency between batches of vector preparation is another obstacle to the gene therapy field, and it is possible that some batches of virus considered “low dose” were better performers than others. For example, batch ID A1454 was used for 2 of the 4 low dose short-term cats, who were euthanized at 16 weeks post treatment at an average CRS of 3.5. This is in contrast to the other two cats in the low dose group, treated with different batches, who were euthanized at the same age with an average CRS of 8.5, similar to the average CRS of the short-term high dose cats (8.33). Given this extreme difference within the low dose short term group, it is possible that cats in the low dose long-term group could have lived longer if they had been treated with a vector batch other than A1454. Improved titering and vector preparation methods will likely improve the consistency of results in future studies.

The variability in longevity, clinical signs, and Hex activity in the long-term groups (of both doses) supports the previously established hypothesis that AAV treatment effectively shifts the phenotype in SD cats from one that imitates the infantile form to one that imitates a later-onset less severe form, such as juvenile. Patients with the infantile form of GM2 possess mutations that render Hex either unable to form or dysfunctional, while juvenile or adult-onset GM2 possess mutations that allow for some Hex to form properly and function, albeit at levels much below normal. By introducing functional copies of *HEXA* and *HEXB* genes to the infantile phenotype imitated by SD cats and causing minor increases in Hex activity, we create a crude representation of a juvenile or adult-onset phenotype. Evidence to support this comes from the variability of lifespan and other clinical signs in cats that respond best to the treatment; the longer the cat lives, the more heterogeneous its lifespan and other clinical signs. This recapitulates human juvenile and adult GM2, in which symptoms and lifespan are more heterogeneous in the patients who have the mildest phenotypes. Therefore, AAV-treated cats provide valuable information not only about response to treatment, but also about later-onset subtypes of GM2.

Table 1. AAV-treated SD cats and their clinical outcomes.

Cat ID	Dose (vg/kg)	AAV Batch ID	Survival (mo)	Final CRS	Fine tremor onset (mo)	Overt tremor onset (mo)	Reason(s) for humane endpoint
11-1326	5E13	A1454	NA*	3	1.1	None	
11-1325	5E13	A1454	NA*	4	1.0	None	
11-1357	5E13	VC4610.2	NA*	8	1.0	None	
11-1493	5E13	A41+A47	NA*	9	None	None	
7-1309	5E13	A1454	9.0	1	1.4	4.9	Overt whole-body tremors
7-1317	5E13	A1454	9.6	1	1.1	8.5	Overt whole-body tremors
7-1320	5E13	A1454	7.8	0	1.1	7.0	Overt whole-body tremors
11-1327	5E13	A1454	6.9	1	1.0	None	Pelvic limb paralysis
11-1416	2E14	VC4610.2	NA*	8	2.6	None	
7-1411	2E14	VC4610.2	NA*	8	1.9	None	
11-1496	2E14	A50	NA*	9	None	None	
11-1329	2E14	VC4610.2	12.6	4	1.2	None	Pelvic limb paralysis
7-1353	2E14	VC4610.2	11.2	6	3.8	None	Pelvic limb paralysis and/or bilateral grade 4/4 luxating patellas
7-1352	2E14	VC4610.2	9.6	5	None	None	Pelvic limb paralysis
11-1355	2E14	VC4610.1+2	16.0	2	0.8	None	Pelvic limb paralysis

CRS: clinical rating score, *indicates cats in the short-term cohort for whom survival was pre-determined by experimental design (16 weeks post-treatment) instead of their response to treatment.

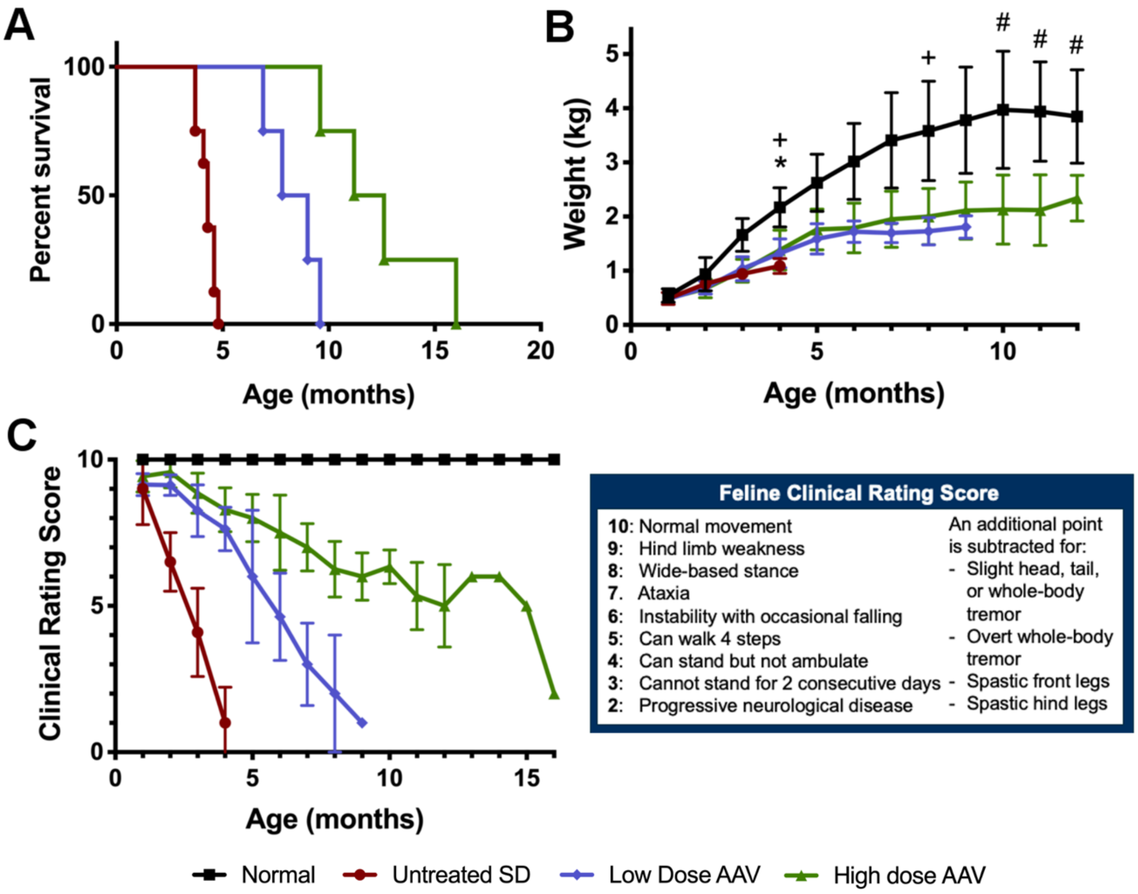

Feline Clinical Rating Score

10: Normal movement
9: Hind limb weakness
8: Wide-based stance
7. Ataxia
6: Instability with occasional falling
5: Can walk 4 steps
4: Can stand but not ambulate
3: Cannot stand for 2 consecutive days
2: Progressive neurological disease

An additional point is subtracted for:
- Slight head, tail, or whole-body tremor
- Overt whole-body tremor
- Spastic front legs
- Spastic hind legs

Figure 1. **Survival and quality of life improve with AAV treatment**. (A) Kaplan-Meier curve demonstrates improved survival with AAV treatment. The lifespan of cats treated with the low dose and high dose nearly doubled and tripled, respectively. (B) Weights of treated cats were partially normalized. * indicates $p<0.05$ untreated SD to normal, + indicates $p<0.05$ low dose AAV to normal, # indicates $p<0.05$ high dose AAV to normal. (C) Neurological clinical rating scores (CRS) indicate dose-dependent delay of neurodegeneration. CRS for the high-dose cohort (green) artifactually increased at 13 months because only one cat with better than average treatment response survived to this age.

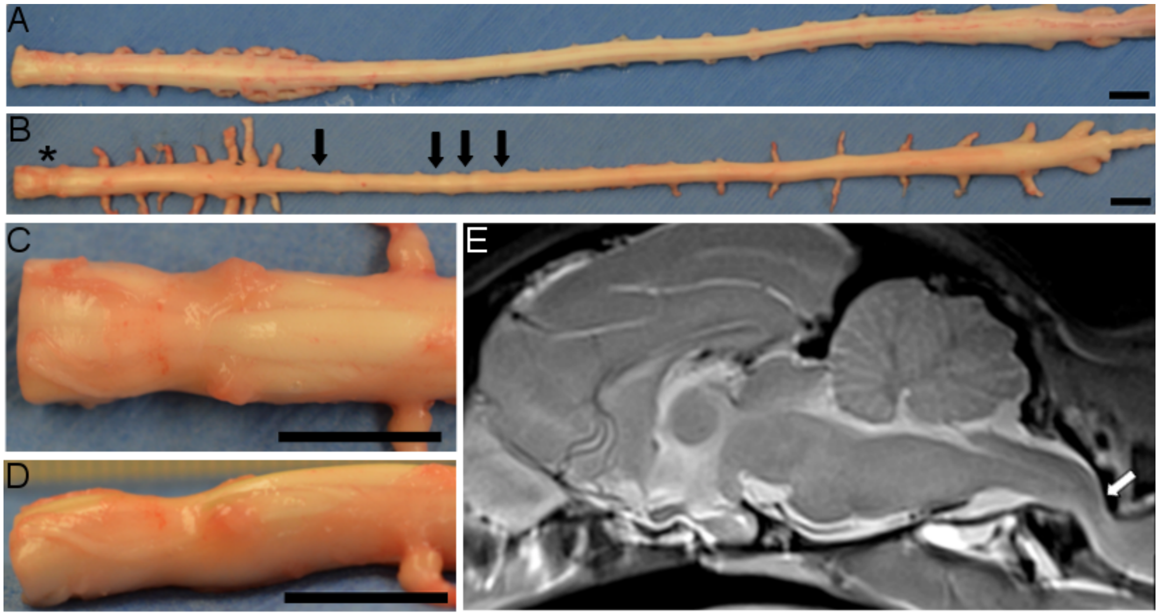

Figure 2. Spinal cord compression in AAV-treated cat. (A) Spinal cord of normal cat at necropsy. (B) Spinal cord of cat 7-1352 at necropsy (9.6 months) with multiple compression lesions, presumably caused by proliferative bone within the vertebral column (not pictured). Black arrows indicate sites of compression at T3, and T7-T9. * indicates most severe site of compression at C1, which is also depicted in (C-E). (C) Magnified view of dorsal surface of C1 compression lesion. (D) Magnified view of left lateral surface of C1 compression lesion. (E) Sagittal view of T2-weighted MRI on midline. White arrow indicates where the thin bright line of the CSF-filled central canal is interrupted at C1 due to spinal cord compression. Scale bar: 1cm.

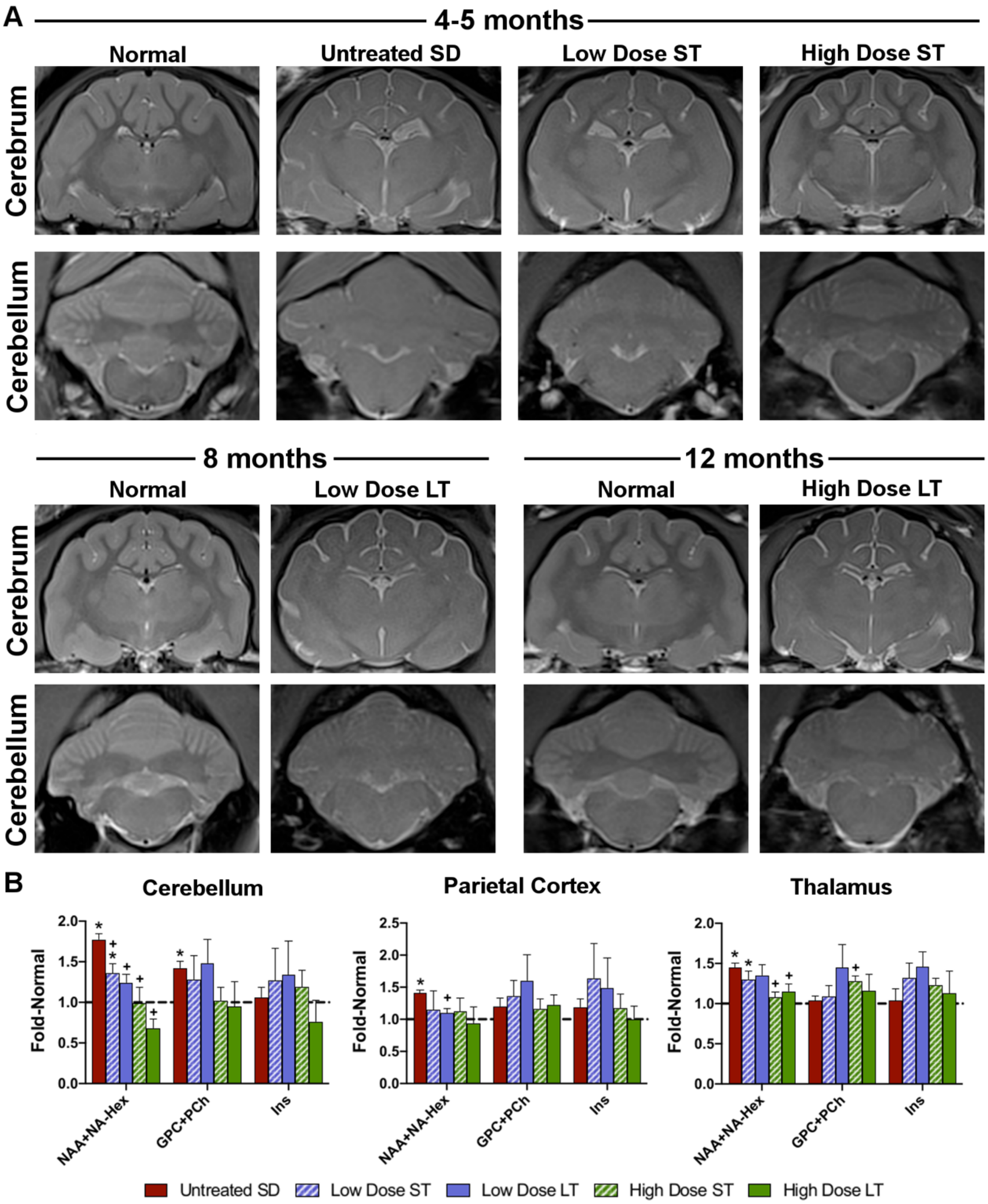

Figure 3. AAV treatment partially normalizes 7T MR images and MRS metabolites. (A) Representative Magnetic Resonance (MR) T2-weighted images acquired with 7 Tesla scanner. In normal cats, white matter is dark gray, gray matter is light gray, and there is minimal bright cerebrospinal fluid (CSF) fluid

around the meninges. The distinction between gray/white matter intensities is decreased or even reversed in untreated SD cats at humane endpoint, indicating hypomyelination and storage in neuron cell bodies. The increased area of CSF signal in untreated SD cats is attributed to generalized atrophy. These pathological changes are mitigated by AAV treatment. (B) MR Spectroscopy (MRS) acquired by 7T scanner. The peak of the neurometabolic marker N-acetylaspartate (NAA) (which merges with N-acetylhexosamine, NA-Hex, a storage product in SD) is significantly increased in all regions of SD cat brains and normalized by the high dose of AAV in the cerebellum and thalamus. Glycerophosphocholine + phosphocholine (GPC+PCh), a measure of membrane turnover and potentially myelin pathology, is significantly increased in the cerebellum of SD cats and normalized in all treatment groups. Myoinositol (Ins) is relatively unchanged in untreated SD cats and all treatment groups. ST: Short-term, LT: Long-term. * indicates $p<0.05$ compared to age-matched normal cats and + indicates $p<0.05$ compared to untreated SD cats.

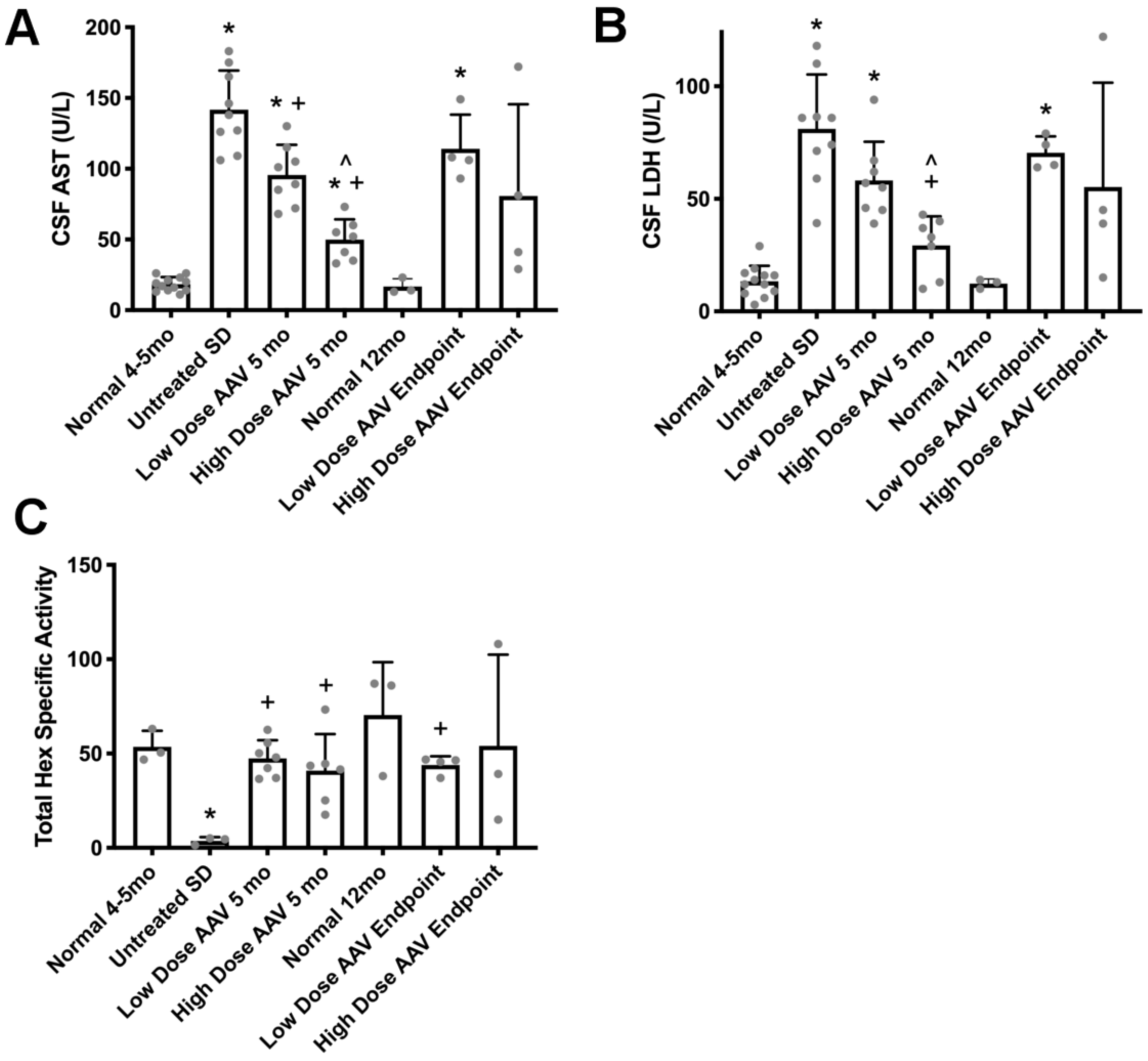

Figure 4. AAV treatment reduces CSF markers of cell damage and increases Hex activity. (A, B) Cerebrospinal fluid (CSF) levels of aspartate aminotransferase (AST) and lactate dehydrogenase (LDH) are significantly increased in SD cats, indicating cell damage within the central nervous system. These levels are significantly reduced in cats treated with the high AAV dose at 5 months. (C) Specific activity of all hexosaminidase isozymes (Total Hex) is significantly decreased in the CSF of untreated SD cats. AAV treatment normalizes Total Hex levels across doses and age groups. * indicates $p<0.05$

compared to age-matched normal cats, + indicates $p<0.05$ compared to untreated SD cats, and ^ indicates $p<0.05$ compared to low dose at same age.

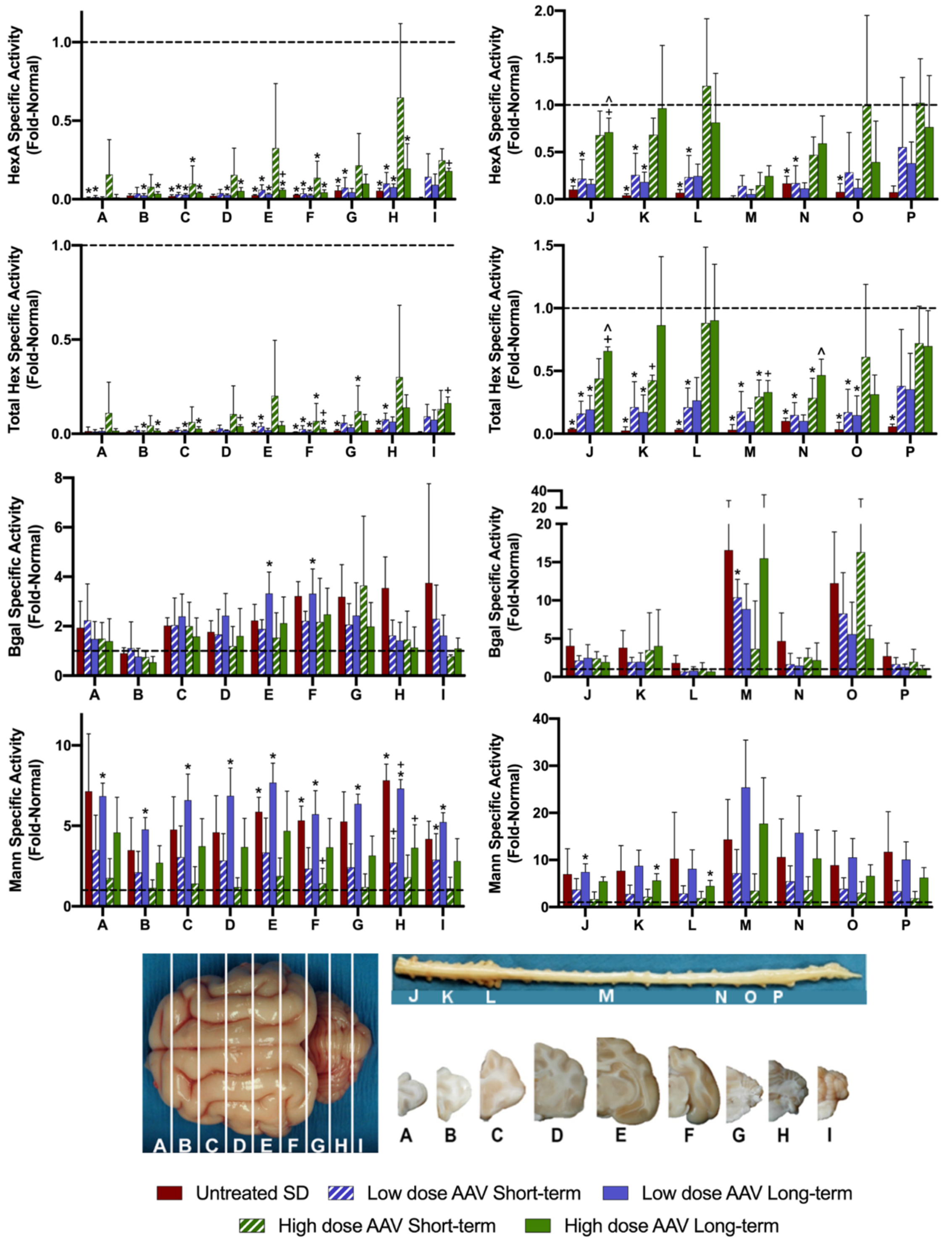

Figure 5. Hex activity increases and Bgal/Mann activity decrease with AAV treatment. Specific activity of the HexA isozyme (HexA) and combined Hex

isozymes (Total Hex) in the brain and spinal cord increases with AAV treatment in a dose-dependent fashion, with the cerebellum, cervical spinal cord, and lumbar spinal cord showing the best response. Specific activity of other lysosomal hydrolases ß-galactosidase (Bgal) and α-mannosidase (Mann) increase to above-normal levels in SD cats in a compensatory attempt to reduce the abnormally high amount of storage material. Reduction of Bgal and Mann levels in AAV-treated cats corresponds with increases in HexA and HexT activity. * indicates $p<0.05$ compared to age-matched normal cats, + indicates $p<0.05$ compared to untreated SD cats, and ^ indicates $p<0.05$ compared to low dose at same age.

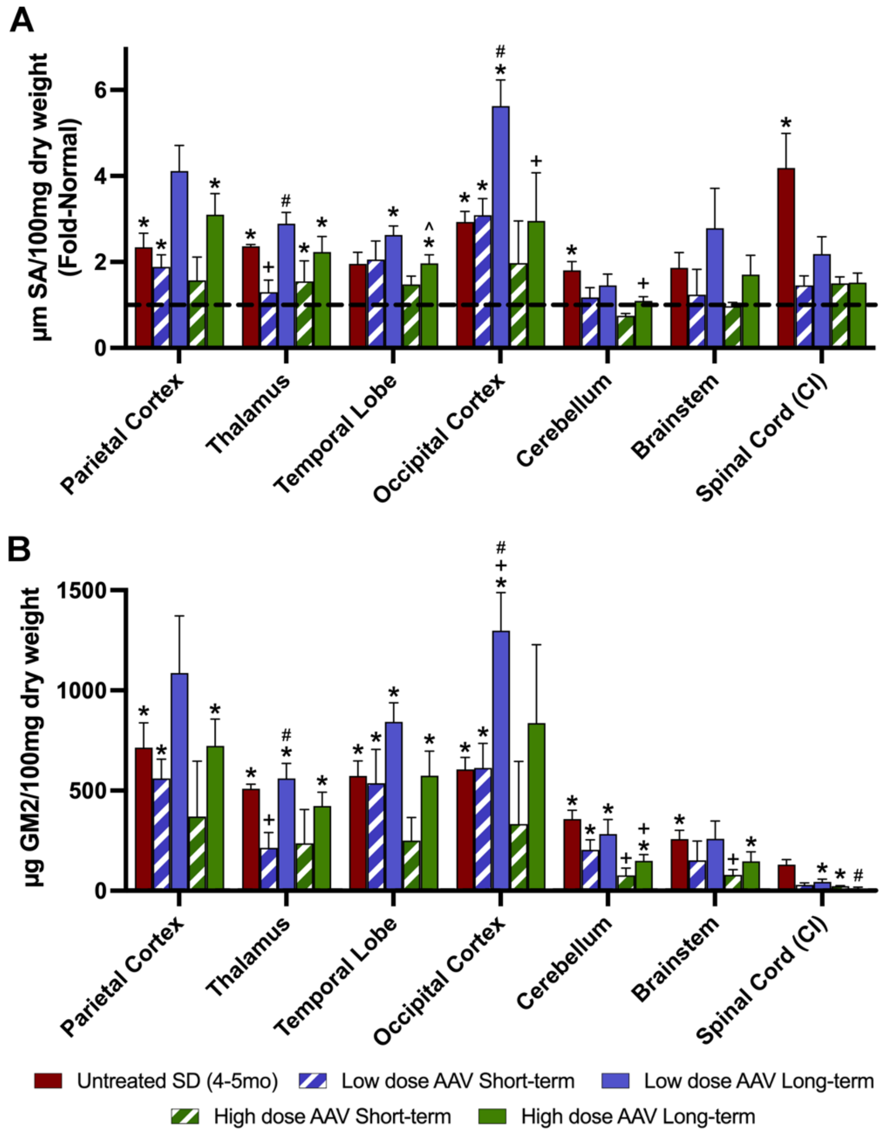

Figure 6. Abnormal accumulation of storage products in SD cats is reduced 16 weeks after AAV treatment but increases long-term. (A) Total sialic acid (SA) and (B) isolated GM2 ganglioside (GM2) is significantly increased above normal levels in most regions. GM2 ganglioside was below detection levels in all normal tissues, and was therefore not depicted here. CI: cervical intumescence. * indicates $p<0.05$ compared to age-matched normal cats, + indicates $p<0.05$ compared to untreated SD cats, ^ indicates $p<0.05$ compared to low dose at same age, and # indicates $p<0.05$ compared to short-term at same dose.

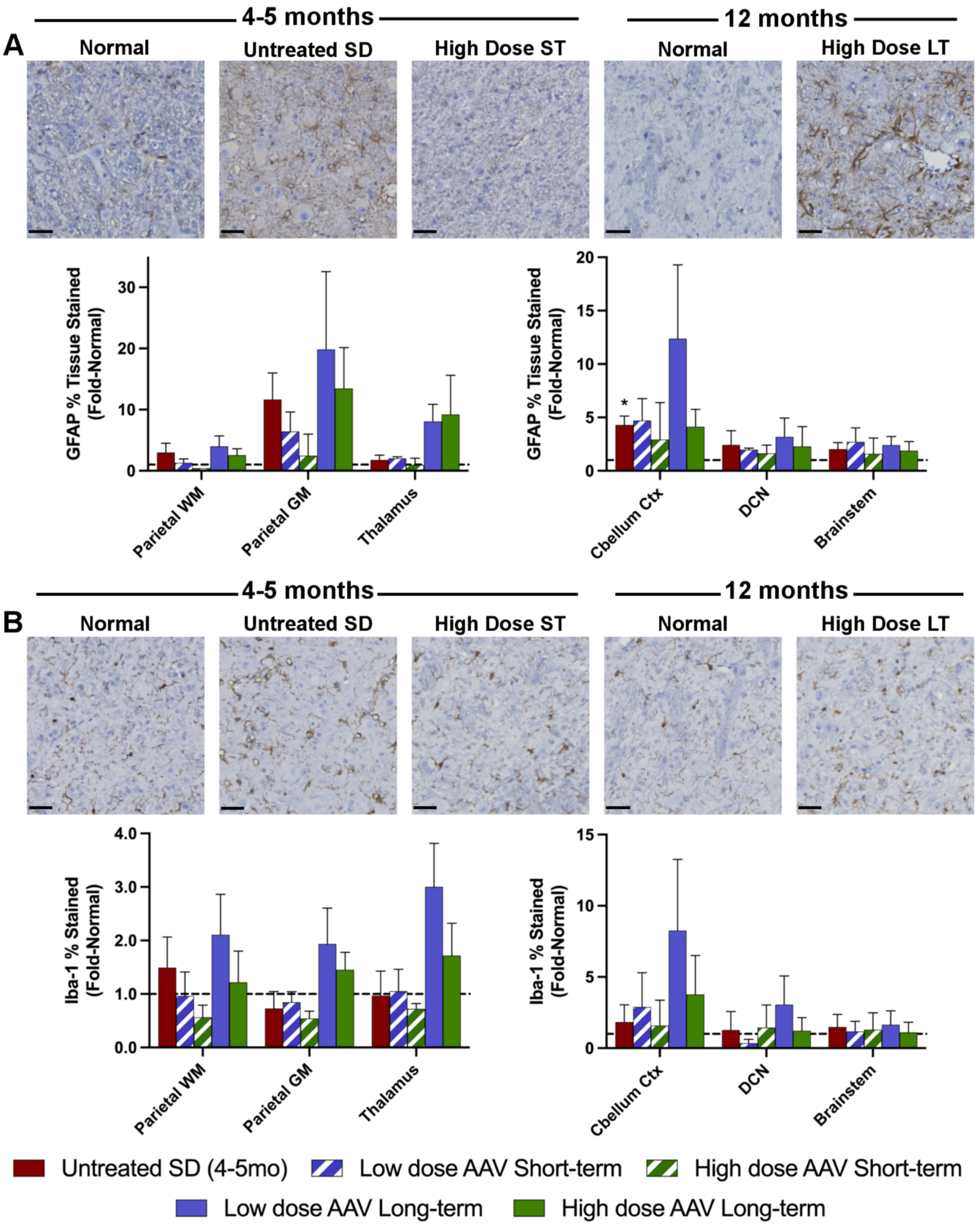

Figure 7. Astrocyte and microglia pathology is partially normalized 16 weeks after AAV treatment but increased in longer-lived cats. Percentage of tissue staining positive for (A) GFAP for astrocytes and (B) Iba-1 for microglia is above normal levels in untreated SD cats, indicating neuroinflammation. In cats

euthanized 16 weeks after AAV treatment, the percentage of stained tissue is partially normalized, while long-term cats in both dosage groups often displayed staining levels well above those of untreated SD cats. Note the increased numbers of astrocytes (A) with activated morphology (thicker processes) and microglia (B) with an ameboid morphology (indicating activation) in untreated SD and high dose LT micrographs. Micrographs at 20x are from the thalamus of representative cats. Scale bar: 20 μm. ST: short-term, LT: long-term, WM: white matter, GM: gray matter, DCN: deep cerebellar nuclei. * indicates $p<0.05$ compared to age-matched normal cats.

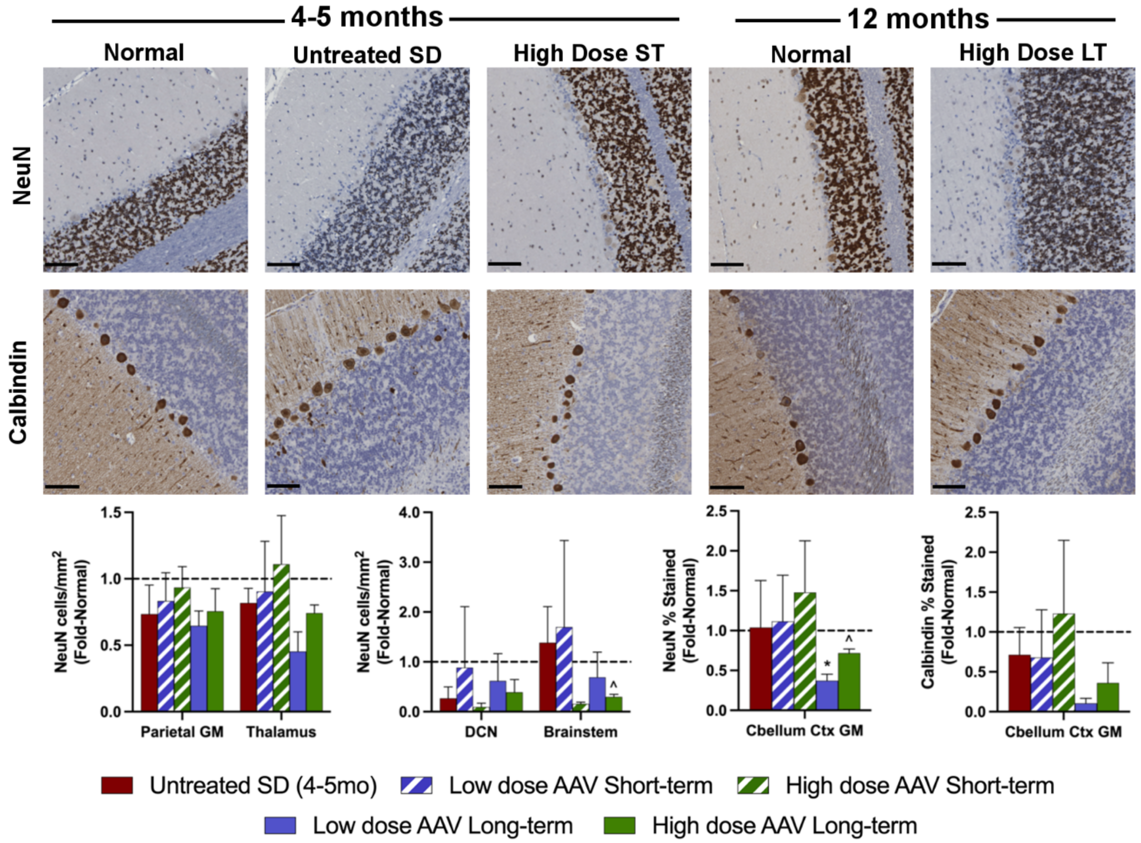

Figure 8. Neuronal loss is inconsistently observed in SD cats, but occurs in longer-lived AAV treated cats. NeuN-positive cell count was below normal in most observed regions of SD cats and dramatically decreased in the long-term cohort of AAV treated cats. For all layers of the cerebellar cortex, % of pixels positive for calbindin staining included axons, dendrites, and cell bodies of Purkinje cells, while % of pixels positive for NeuN staining included the nuclei of non-Purkinje neurons. Micrographs at 20x are from the cerebellar cortex of representative cats. Scale bar: 20 µm. ST: short-term, LT: long-term, GM: gray matter, DCN: deep cerebellar nuclei. * indicates $p<0.05$ compared to age-matched normal cats, ^ indicates $p<0.05$ compared to low dose at same age.

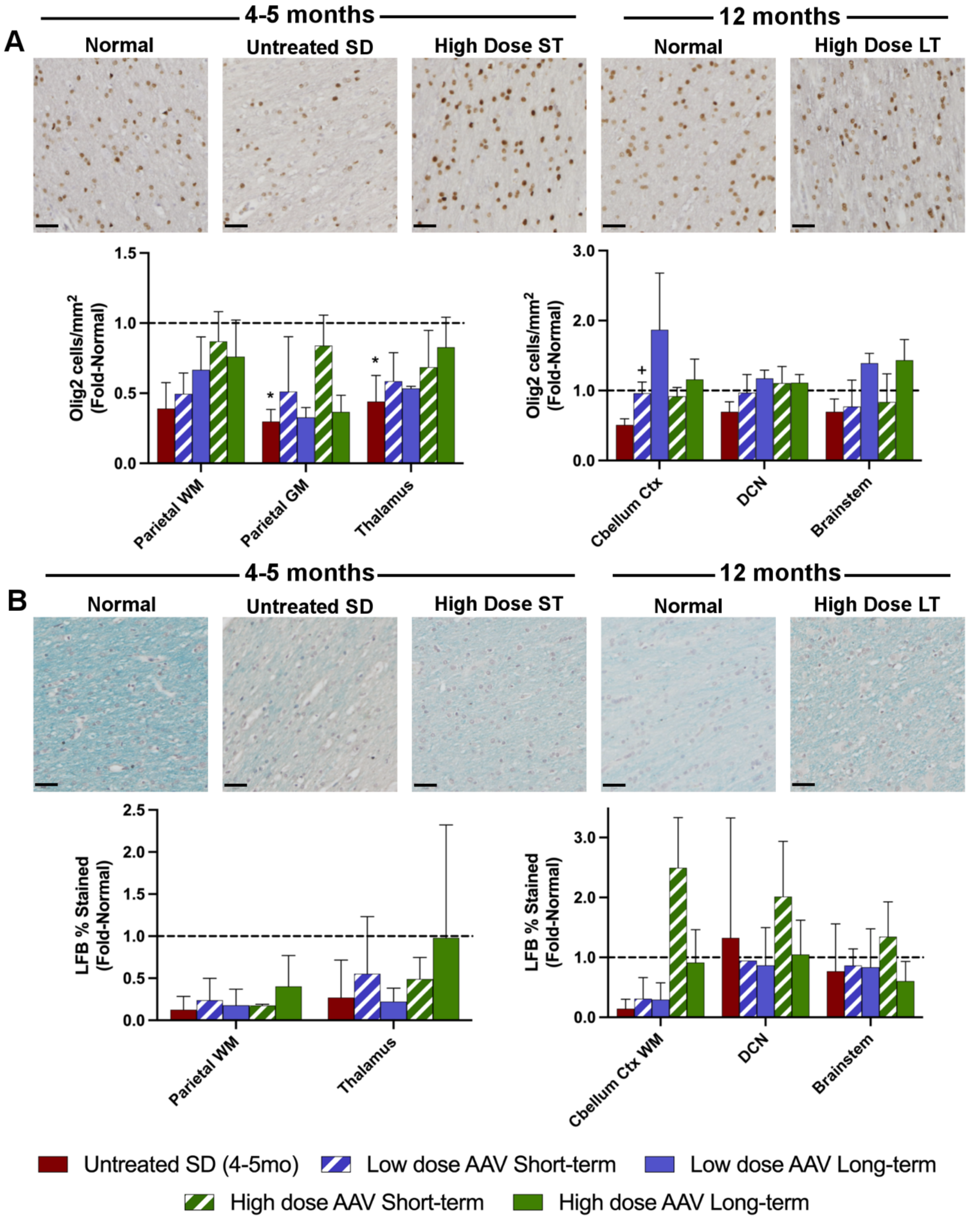

Figure 9. **Myelin deficits in SD cats are partially normalized through AAV treatment.** (A) Oligodendrocytes staining positive for Olig2 and (B) percentage of tissue staining positive for Luxol Fast Blue (LFB) are below normal levels in SD cats and partially restored in AAV-treated cats. Micrographs at 20x are from the

parietal cortex white matter of representative cats. Scale bar: 20 μm. ST: short-term, LT: long-term, WM: white matter, GM: gray matter, DCN: deep cerebellar nuclei. * indicates $p<0.05$ compared to age-matched normal cats, + indicates $p<0.05$ compared to untreated SD cats.

Chapter 2

Normal feline myelinogenesis and early myelin deficits in cats affected by Sandhoff Disease

Anne S Maguire[1,2], Douglas R Martin[1,2]

[1]Scott-Ritchey Research Center, [2]Department of Anatomy, Physiology & Pharmacology, College of Veterinary Medicine, Auburn University, Auburn AL 36849, USA

Introduction

GM1 and GM2 gangliosidosis (GM1 and GM2, respectively) are neurodegenerative lysosomal storage diseases that result in the death of affected children before 4 years of age. GM1 is caused by the absence of ß-galactosidase and subsequent accumulation of GM1 in neuronal lysosomes, while the pathogenesis of GM2 is a result of the absence of ß-hexosaminidase (Hex) and subsequent accumulation of GM2 ganglioside in neuronal lysosomes. There are two major forms of GM2 gangliosidosis: Sandhoff Disease (SD) and Tay-Sachs Disease (TSD), which present with very similar clinical symptoms. Storage lesions in the gangliosidoses result in a cascade of pathological effects throughout the body, but primarily in the central nervous system (CNS). A feline model of SD is a valuable intermediate step between testing therapeutics in mice and human clinical trials.

Deficits in white matter tracts have often been observed in GM1, GM2, and other closely related LSDs, but few studies have investigated their origin. In any CNS disease involving myelin deficits, there are three possible mechanisms for their origin: dysmyelinogenesis (failure to form properly), primary demyelination (destruction after proper formation), or secondary demyelination (loss after axonal degeneration). In the last review of this subject (in 1999[35]), Folkerth concluded that dysmyelinogenesis was likely the leading mechanism in white matter pathology for most LSDs. This was supported by the fact that white matter tracts that typically myelinate “early” (initiated prenatally) were less affected than tracts whose myelination is initiated postnatally. This led to the overall impression that myelin development in affected patients was “arrested”, mirroring that of a normal pattern expected for a younger person, as opposed to formed normally and destroyed (demyelination). However, further investigation into the pathogenesis of the dysmyelinogenesis was stymied by the lack of details on oligodendrocyte appearance and numbers. Most primary studies simply noted myelin pallor and attributed it to axonal degeneration secondary to storage deficits, even though axonal spheroids (evidence of axonal degeneration) are rare in GM1 and GM2 cases.

Though there are clearly more steps to be delineated in the pathological cascade of dysmyelinogenesis in LSDs, few studies since the 1999 review by Folkerth have investigated the details necessary to accomplish this. In 2004, van der Voorn et al.[49] noted oligodendrocyte cell death along with decreased myelin protein markers and axonal degenerative changes in infantile GM1, but only examined the frontal lobe. Most recently, these investigations have occurred in tandem with studies evaluating the efficacy of adeno-associated viral (AAV) gene therapy, in some cases introducing previously unpublished information in the context of establishing baselines for untreated controls. Cachon-Gonzalez et al. in 2014[50] observed degenerative changes to axons and decreased levels of myelin proteins and mRNA in most regions of the CNS of SD mice, and drew intriguing parallels between SD mice and the *twitcher* mouse model of Krabbe disease. Gray-Edwards et al. in 2020[40] found that a decrease in oligodendrocyte number did not occur in GM1 cats, though oligodendrocyte pathology was clearly visible ultrastructurally.

Because the most severe forms of LSDs result in a conflict between neurodevelopment and neurodegeneration, any comprehensive examination of myelin pathology in LSDs should consider two major components: differences that may occur between developmental timepoints (temporal), and those that occur across regions of the CNS (spatial). Though several studies have considered the spatial component and examined multiple regions of the CNS, incorporation of the developmental component is more difficult, especially in human patients, due to the scarcity of appropriate *in vivo* methods. Therefore, SD cats are an excellent resource because they are appropriate models of the human CNS size, complexity, and disease progression. However, there are no comprehensive studies in the literature regarding normal myelinogenesis in cats, much less myelinogenesis complicated by neurodegenerative LSDs. The purpose of this study is to characterize myelin development in normal and SD cats, spatially and temporally, through quantification of mRNA, Olig2-positive cells, and qualitative evaluation of LFB staining. By documenting these parameters, we hope to further elucidate the pathogenic cascade of myelin deficits in SD and provide baseline information for future gene therapy studies.

Methods

1.0 Animals

A breeding colony of SD cats is maintained at Scott-Ritchey Research Center at Auburn University, and all experiments in this study were approved by its Institutional Care and Research Committee. Cats were euthanized with cardiac injection of pentobarbital and perfused transcardially with cold saline. For the RT-qPCR experiment, n=3 for all cats. For the Olig2 and LFB experiment, n=3 for cats at the 1 month and 2 month age points and n=4-5 for cats at 4-5 months of age.

2.0 Tissue Preparation

Brains were divided into 9 transverse blocks of 0.6 cm from the frontal pole through the cerebellum. Blocks from the left hemisphere were halved to 0.3 cm and either flash frozen in liquid nitrogen or fixed in 10% formalin. Frozen tissue was stored at -80°C and used for the RT-qPCR experiment. Formalin-fixed tissue was embedded in paraffin blocks and used for Luxol Fast Blue (LFB) or Olig2 staining.

3.0 RT-qPCR

3.1 RNA Isolation and cDNA Creation

Pieces of frozen tissue (50-100ng) were cut from the relevant region and manually homogenized in 1 mL RiboZol RNA extraction reagent (VWR Life Science, Radnor, PA, USA). Chloroform (200 µL) was added to the solution, which was shaken vigorously before incubating at room temperature for 3 minutes. After centrifugation at 4°C for 15 minutes, the upper aqueous layer was transferred to a new collection tube, and an equal volume of 70% ethanol was added. This solution was transferred in 700 µL increments to RNeasy MinElute Columns (Qiagen, Germantown, MD, USA) and the remaining protocol was identical to the protocol included in the RNeasy Micro Kit (Qiagen). RNA concentration was measured on a NanoDrop OneC (Thermo Fisher Scientific, Pittsburgh, PA, USA) and stored at -80°C. cDNA was created using Invitrogen SuperScript III first-strand synthesis system (Thermo Fisher Scientific) and concentration measured on the NanoDrop One C.

3.2 Primer and Standard Curve Preparation

The following primers were ordered from IDT (Integrated DNA Technologies, Coralville, IA, USA) and are shown in the 5' to 3' direction:

- PDGFRA Forward: CCACTCACTCCATCTCTCAGGT
- PDGFRA Reverse: GGCAGGAGATTAGGCTCGGT
- NG2 Forward: CACGATGGGAGTGAGACGCT
- NG2 Reverse: TGAAGGTCACCGGATGGCTC
- Olig2 F TCTAAGTGCATCCACAGAGGC
- Olig2 R CCGAGGGATAGTCGCAGCTC
- PLP1 F CTTTGGAGCGGGTGTGTCAT
- PLP1 R ACGGTCAGGGCATAGGTGATG
- MBP F GGCTCAAGCAGAGAAGGAGCC
- MBP R GCCATAGTGGGCAGTTCTCG
- GAPDH F: CCTCATTGACCTCAACTACAT
- GAPDH R: GAAGATGGTGATGGGCTTT

The oligodendrocyte and myelin-related primers were PDGFRA (platelet-derived growth factor alpha), NG2 (neural-glial antigen 2), Olig2, PLP1 (proteo-lipid protein 1), and MBP (myelin-basic protein). They were designed using Primer-Blast (NCBI, National Center for Biotechnology Information, Bethesda, MD, USA), while the GAPDH (glyceraldehyde-3-phosphate-dehydrogenase) primer has been previously validated in cats by this research group. Primers were reconstituted to 400μM and stored at -20°C. Conventional PCR was performed with each primer on a representative sample using a GoTaq Flexi DNA Polymerase kit (Promega, Madison, WI, USA), and the DNA product isolated from the gel using an EZNA Gel Extraction kit (Omega Bio-Tek Inc, Norcross GA, USA). DNA concentration was measured on the Nanodrop OneC and used to calculate molar concentrations that resulted in 1E8, 1E6, 1E4, and 1E2 copies for use in the qPCR standard curve. The DNA product was stored at 1E10 mol/μL at -20°C.

3.3 qPCR

cDNA samples (100 ng per well) were run in duplicate (or triplicate for troubleshooting) using SYBR Green master mix (Thermo Fisher Scientific) on 96-well PCR plates. Each plate was restricted to one primer and one brain region. Plates were run on a QuantStudio3 (Applied Biosystems, Thermo Fisher Scientific), with annealing temperature of 60°C. Copy number was extrapolated from the primer-specific standard curve from each plate.

4.0 Luxol Fast Blue Staining

Slides underwent a rehydration series of 8 minutes in Hemo-D (Scientific Safety Solvents, Keller, TX, USA) or xylene (3x), 2 minutes in 100% ethanol (2x), 2 minutes in 95% ethanol (2x), 2 minutes in distilled water, then incubated overnight at room temperature in Luxol Fast Blue solution (0.1% in 95% alcohol with acetic acid, Electron Microscopy Sciences, Hatfield, PA, USA). In groups of 2 or 3 with at least one normal sample, slides were dipped in lithium carbonate (0.05%, Diagnostic BioSystems, Pleasanton, CA, USA) and 70% ethanol until the gray matter was clear. After a rinse in distilled water, slides were counterstained with Mayer's Hematoxylin (Electron Microscopy Sciences) for 3 minutes, followed by a 3-minute rinse in running water. Slides dried overnight at room temperature and were coverslipped the following day.

5.0 Immunohistochemistry

Slides were dehydrated in the same series as for LFB staining, then underwent antigen retrieval with Antigen Decloaker (Biocare Medical, Concord, CA, USA) in a decloaking chamber (Biocare Medical). After rinsing in distilled water, slides were loaded into an IntelliPath FLX slide stainer (Biocare Medical). All reagents were manufactured by Biocare Medical unless otherwise noted:

1. Block: IP FLX Peroxidase, 5 minutes
2. Block: IP FLX Background Punisher, 5 minutes
3. Primary antibody: From Abcam (Cambridge, MA, USA), 1:200 dilution into Da Vinci Green Diluent, 30 minutes

4. Secondary antibody: MACH 2 Rabbit HRP-Polymer, 30 minutes
5. Chromogen: Betazoid DAB, 5 minutes
6. Counter-stain: Tacha’s Auto Hematoxylin, 3 minutes

- Buffer wash throughout: TBS Auto Wash Buffer

Slides dried overnight at room temperature and were coverslipped the following day.

6.0 Image Acquisition of Stained Slides

A Keyence BZ-X810 (Keyence, Itasca, Illinois, USA) was used to acquire all images. After brightness correction and scout scans at 4x, relevant regions were outlined at 20x and individual images were acquired. Images were stitched together with the built-in software and saved in the Big TIFF format. Files were imported into QuPath software[85] version 0.2.3 where they were qualitatively assessed, with representative images exported for inclusion in figures. Images for the 1 month and 2 month age groups for Figure 3 were taken directly with the Keyence at 20x.

7.0 Quantification of Stained Slides

After images were acquired and imported into the QuPath software (described above), algorithms were designed for each stain and tested on 2-3 images from cats in different treatment groups. Because Olig2 is a nuclear stain, the algorithm was designed to count the number of stained nuclei per mm^2 by using the cell detection function based on optical density, then applying an object classification to detected cells to differentiate DAB-positive cells from hematoxylin-positive cells if necessary. Algorithm specifications are detailed below.

The first step in the analysis of each image was to manually input the magnification as 20x and pixel length as 0.2 x 0.2 µm, since that information was not imported automatically with the metadata attached to each slide. Second, a stain vector was applied, to optimize the software's differentiation between hematoxylin and DAB (stain vectors provided below). Third, regions of interest (parietal cortex white matter/gray matter, thalamus, cerebellar cortex white matter/gray matter, DCN, brainstem) were hand-drawn using the brush and wand tools. Fourth, the algorithm was applied and the resulting data manually recorded in a Microsoft Excel file. The hematoxylin shade was dramatically different between two batches of staining (first batch with the 4-5 month cohort and second batch with the 1 month and 2 month cohorts), so slides from the first batch were repeated in the second to determine a correction factor and allow comparison across batches.

- Stain vectors:
    - Hematoxylin: 0.739 0.538 0.405
    - DAB: 0.452 0.589 0.67
    - Background: 240 240 240
- Cell detection:
    - Detection image: Optical density sum
    - Requested pixel size: 0.2 µm

  - Background radius: 10 μm
  - Median filter radius: 0 μm
  - Sigma: 1.0 μm
  - Minimum area: 6 μm^2
  - Maximum area: 400 μm^2
  - Threshold: 0.25
  - Maximum background intensity: 2.0
  - Split by shape: true
  - Exclude DAB: false
  - Cell expansion parameters: 0 μm
  - Include cell nucleus: true
  - Smooth boundaries: true
  - Make measurements: true
- Object classification
  - Channel filter: DAB
  - Measurement: DAB OD Mean
  - Threshold: 0.08
  - Above: Positive
  - Below: Negative

8.0 Data Analysis and Statistics

All statistical analyses and graphs were generated with GraphPad Prism version 9.1.2 for Mac OSX (GraphPad Software, La Jolla California USA, www.graphpad.com). All tests were Welch's ANOVAs with alpha values of 0.05 and Dunnett's T3 multiple comparisons test for post-hoc analyses. Post-hoc tests included every normal age group against each other and every SD age group against each other, plus normal versus SD for every age group.

Results

The mRNA for proteins known to appear early in the myelination process (PDGFRA, NG2) is highest in the younger cohorts of normal cats, then decreases steadily in older cats (Figure 1). The opposite pattern is observed in PLP1, known to be present later in the myelination process. MBP, which also appears late in the myelination process, has more consistent mRNA levels throughout the age groups studied. Olig2 mRNA levels fit the expected pattern of consistency across all age cohorts. Similar patterns were noted in SD cats, though their mRNA levels are usually below those of their normal counterparts. GAPDH mRNA levels, which were measured as a reference, were similar across all age groups, though differences were observed between brain regions.

Cells staining positive for Olig2 were at similar numbers across all age cohorts of normal cats, as expected for the marker Olig2 which is known to be present throughout development. In the SD cat brain at all time points, Olig2-positive cell numbers were between 30-40% of normal in the parietal cortex white matter, 30-55% in the parietal cortex gray matter, 25-45% in the thalamus, 35-70% in the cerebellar cortex, and 40-70% in the DCN and brainstem (Figure 2). In the cerebellar cortex, DCN, and brainstem of 2-month-old cats, a dip in oligodendrocyte count appeared at 2 months of age in both normal and SD cats. Most LFB slides exhibited regions of uneven staining that eliminated the possibility of quantification, but qualitative evaluation of properly-stained areas was possible (Figure 3). Myelin development was more advanced in the cerebellar cortex than the parietal cortex of normal cats at 1 month and 2 months of age, at which point they appeared to have similar LFB stain intensity. Notable pallor was observed in the cerebellum of SD cats starting at 1 month of age, while similar pathology in the parietal cortex was not apparent until 4-5 months (end stage).

Discussion

This study was successful in validating 5 new primers for use in RT-qPCR of mRNA related to oligodendrocytes and myelin in feline tissue, though there were some limitations. The copy number for most samples run with the PDGFRA primer was <100, which is below the lowest value on the standard curve. Therefore, the accuracy of the copy number for each sample is questionable, and unacceptable levels of variability may have been introduced. For the Olig2 primer, the melt curves for the samples that constitute the standard curve had a small “shoulder” leading into the peak that was unresponsive to troubleshooting attempts such as procuring DNA from a different tissue and adjusting the melting temperature. In addition, thalamus samples run with several different primers often had extreme variability between duplicates. Plates were repeated in triplicate to determine values that were most likely to be accurate, but the reason for the initial variability is still unknown. A combination of these last two limitations could have led to the extremely low copy numbers observed in the thalamus samples run with the Olig2 primer, and these data should be analyzed cautiously.

PDGFRA and NG2 (also known as also known as CSPG4, chondroitin sulfate proteoglycan 4) are both expressed in OPCs (oligodendrocyte precursor cells), the first cells in the oligodendrocyte differentiation lineage[27,96]. Co-expression of the receptor PDGFRA and proteoglycan NG2 appear to be crucial for OPCs to respond to PDGF (platelet-derived growth factor), which stimulates mitosis[97]. We found expected levels of mRNA in normal cats, with both markers highest in younger cats when maximum OPC numbers are expected to be present. Despite the prevalence of using these markers, especially NG2, as markers of early oligodendrocytes, no study to date has quantified the DNA, mRNA, or proteins of PDGFRA or NG2 in GM1 or GM2. This study demonstrated that deficits in SD cats begin around 1 month of age in the mRNA of NG2 in the parietal cortex and thalamus, and are present in both markers across all four regions by 2 months of age.

PLP1 and MBP are well-established markers of mature oligodendrocytes and myelin, due to their high prevalence in mature myelin sheaths. We found that PLP1 follows the expected pattern of its mRNA levels increasing with the age of normal cats, except in the cerebellum and brainstem. This could be because these regions are the first to complete the myelination process, and therefore may begin downregulating mRNA production while the other myelinating regions are still increasing production. MBP also followed an unexpected pattern of its mRNA levels reducing with age in all regions studied. This could be due to similar reasons as the PLP1 reversal, and could be complicated by the fact that MBP is transported post-transcription to be translated at the cell membrane[98]. The measurement of protein through Western blots and/or IHC would therefore be important to gain more information into the normal mature myelin development process.

To date, only two studies have investigated these markers in GM1 and GM2. In 2004, van der Voorn et al. found decreases in IHC staining of both MBP and PLP1 in the frontal lobe in two cases of human infantile GM1, with PLP1 having a more severe reduction than MBP[49]. In 2014, Cachon-Gonzalez quantified mRNA of PLP1 through RT-qPCR in end-stage SD mice and found abnormally low levels throughout the CNS. Surprisingly, they also found reductions in CGT (UDP-galactose:ceramide galactosyltransferase), another marker of mature myelin, in the youngest age investigated (5 weeks). In this study, we observed a similar pattern of deficits in SD cats in that PLP1 and MBP were deficient in all regions at all ages studied.

The two major functions of Olig2 are to initiate OPC differentiation and complete development into mature oligodendrocytes[99,100], and it is therefore used as a marker of oligodendrocytes across all developmental stages. To date, no studies have examined Olig2 mRNA in the gangliosidoses. We found that Olig2 mRNA levels in normal cats are similar across all ages examined in the parietal cortex and thalamus. In the brainstem, the copy number decreases with age in a similar pattern to MBP in the cerebellum. This could be due to the early maturation of myelin in the brainstem compared to the other regions resulting in less need for upregulation of Olig2. Intriguingly, of the 5 myelinogenesis-related primers examined, SD cats demonstrated the least dramatic reduction compared to normal controls in Olig2 across all ages and regions, even showing an increase in most regions at 2 weeks of age.

This is in sharp contrast to the Olig2 IHC data, in which substantial reductions in Olig2-positive cells were observed across all ages and regions examined. This extreme difference between the Olig2 mRNA and protein quantification results could be due to pathology occurring during the translation process, and is a promising area for future study. Statistical significance was achieved in the parietal cortex and thalamus between normal and SD cats at 4-5 months of age but not in the other age groups despite similar numerical differences, likely because n=5 (normal) and n=4 (SD) for the 4-5 month cohort, while n=3 for the other cohorts. Similar to the mRNA results, Olig2-positive cells remained relatively consistent across age groups for both normal and SD cats. One exception is a drop in the cerebellar cortex, DCN, and brainstem at 2 months of age, for which there is no obvious explanation.

Though several limitations precluded meaningful quantification of LFB-stained slides in this study, useful information can be extracted from qualitative analysis. LFB staining intensity can be dampened by prolonged periods of formalin fixation time, which several of the tissues in this study underwent. In addition, appropriately differentiated staining that was evenly distributed across the entire tissue section was very difficult to achieve on sections from younger cats (1 or 2 months) due to their small size and reduced gray/white matter distinction. Despite these limitations, it was apparent that the cerebellum, DCN, and brainstem myelinate before the parietal cortex and thalamus, as demonstrated by increased blue intensity in these regions. The obvious LFB pallor in SD cats extends observations by Folkerth[35] that the myelinogenesis process is “arrested” at some point in the LSD pathogenesis before existing myelin starts to become destroyed as the disease approaches end stage. This hypothesis is best examined in LFB images from the cerebellar cortex, in which the blue intensity in the 2 month old SD cat looks similar to that of the 1 month old normal cat, but the 4-5 month old cat (SD end stage) has the lowest LFB intensity of all.

In conclusion, this study has established baseline levels of mRNA and protein (IHC) for common myelinogenesis markers in developing normal and SD cats. Deficiencies in the mRNA levels of SD cats were apparent in most ages and regions examined, appearing as early as one month for some OPC markers. The number of Olig2-positive oligodendrocytes was dramatically reduced in SD cats starting at the youngest age examined (1 month). Future studies could explore the source of myelinogenesis pathology further by completing the mRNA and protein profile for these markers to determine if translation deficiencies are present. Extensive investigation of any oligodendrocyte and myelin sheath pathology present using transmission electron microscopy would be informative on a cellular level. The characterization of normal and SD cats across developmental ages could be expanded by adding magnetic resonance (MRI), and RT-qPCR/IHC staining of markers for inflammation and neuronal degeneration. By continuing to elucidate white-matter-specific pathology that occurs, we hope to continue to improve therapeutic efforts for SD and other devastating neurodegenerative diseases.

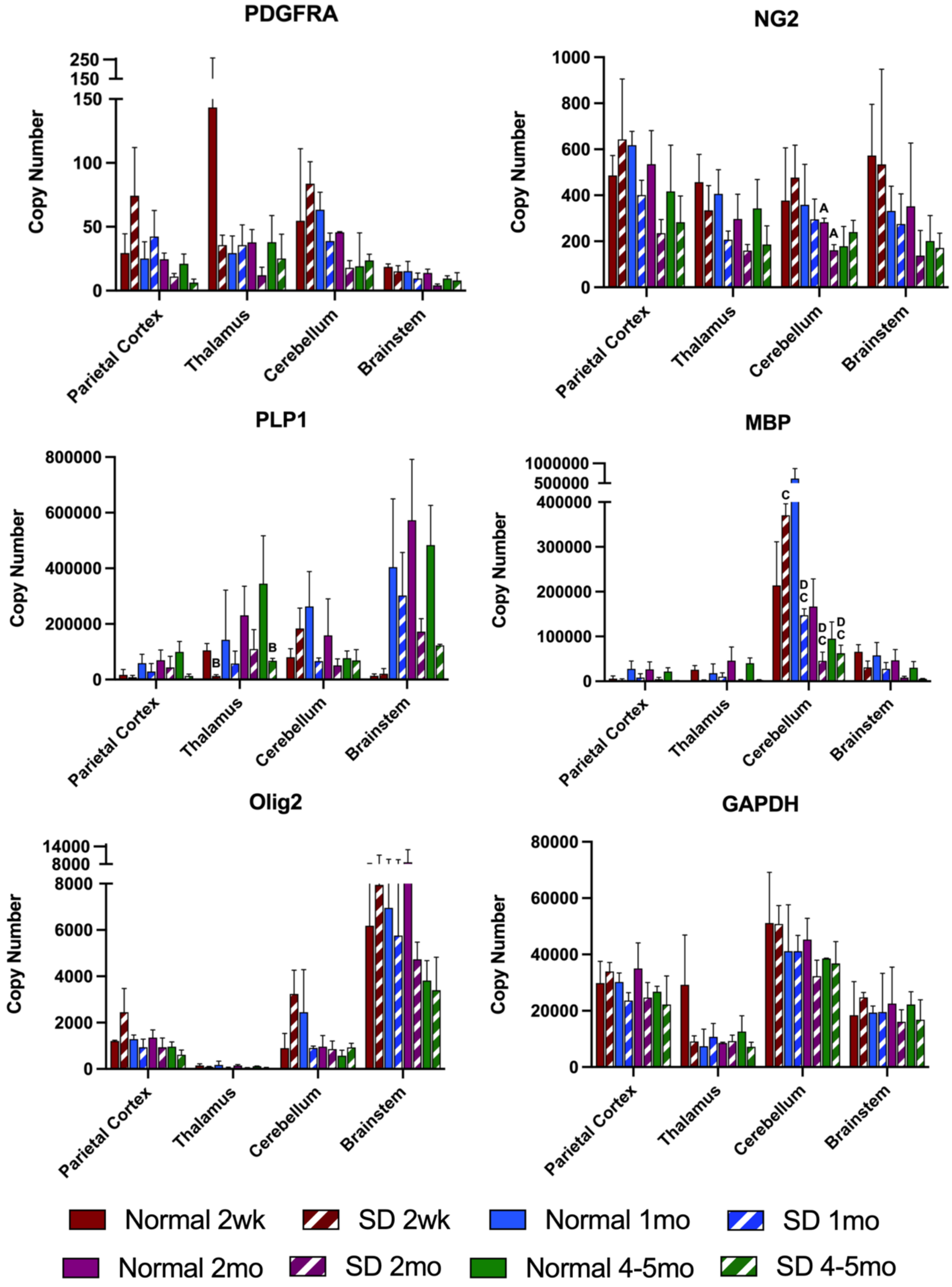

Figure 1. Copy number for mRNA markers of myelination in developing normal and SD cats. Results of RT-qPCR across 4 regions in 4 different age

groups for 5 myelination primers (with GAPDH as reference). PDGFRA: platelet derived growth factor receptor alpha, NG2: neuron-glial antigen 2 (also known as CSPG4, chondroitin sulfate proteoglycan 4), PLP1: proteolipid protein 1, MBP: myelin basic protein, GAPDH: glyceraldehyde-3-phosphate-dehydrogenase. Matching letters indicate $p < 0.05$.

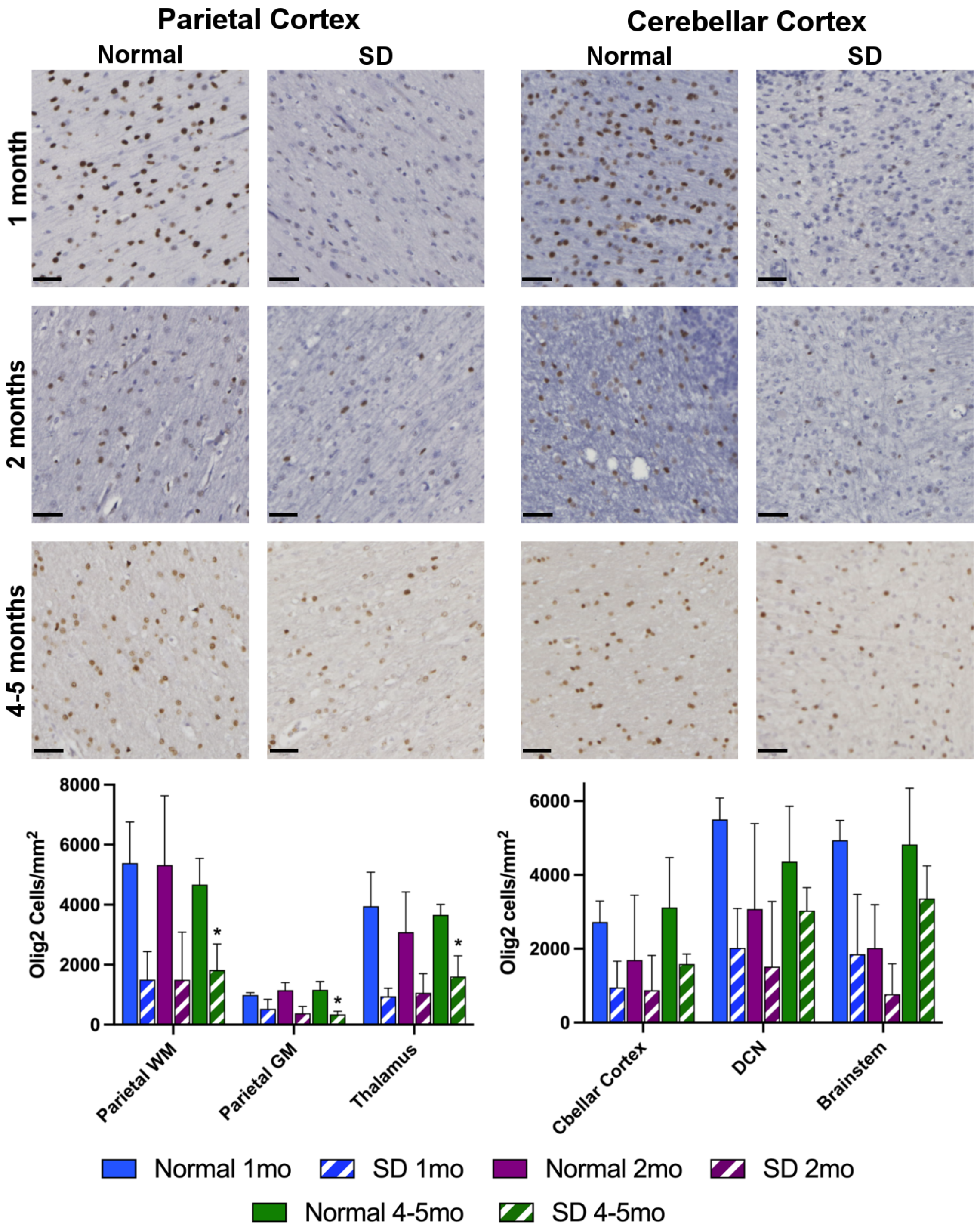

Figure 2. **SD cats have fewer Olig2-positive cells than their age-matched controls throughout development**. Quantification of whole slides reveal consistent numbers of Olig2-positive cells throughout the development of normal

cats, but dramatically fewer oligodendrocytes in SD cats. Slides for the 4-5 month age group were counter-stained with a less intense hematoxylin, which was corrected for in the quantification methods. Scale bar: 20 μm. WM: white matter, GM: gray matter, DCN: deep cerebellar nuclei. * indicates $p<0.05$ compared to age-matched normal cats.

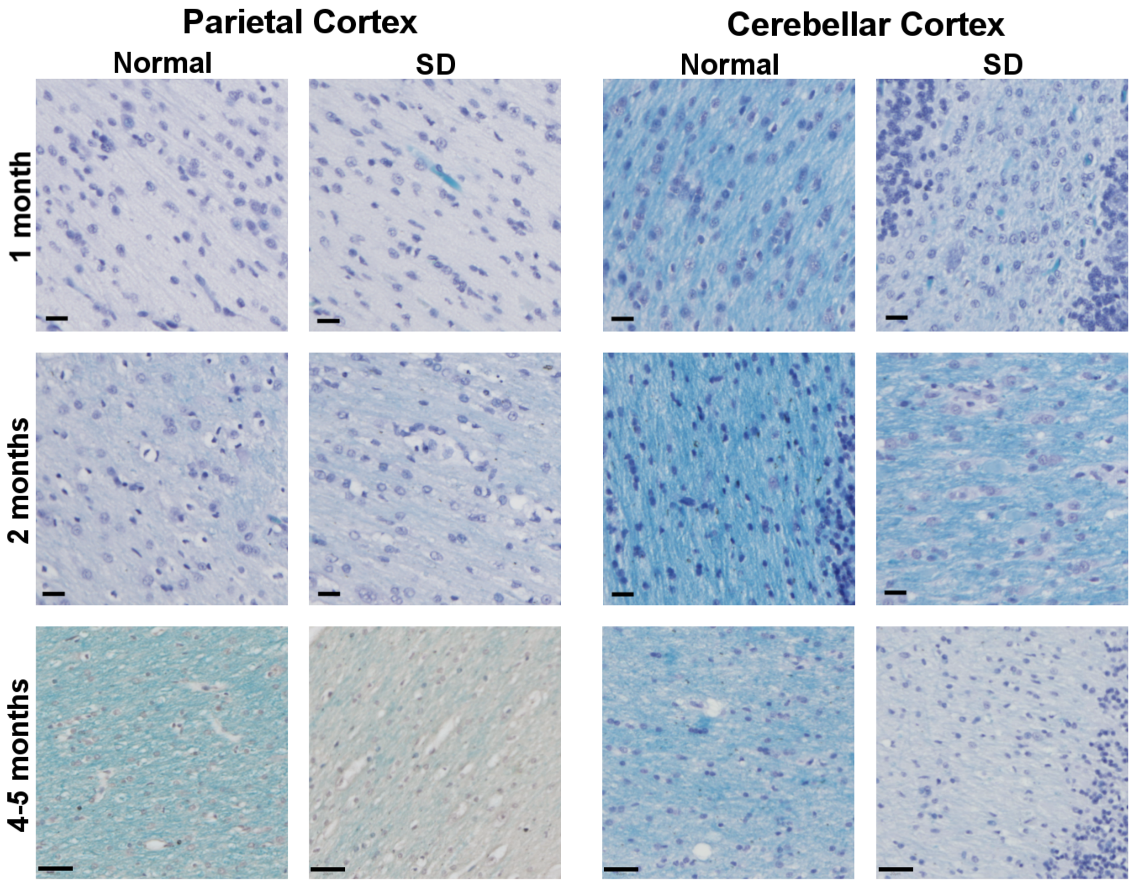

Figure 3. LFB Staining over the course of development in normal and SD cats. Myelin development is more advanced in the white matter of the cerebellar cortex than of the parietal cortex of normal cats at 1 month and 2 months of age. SD cats have noticeably deficient LFB staining in the cerebellum starting at 1 month of age, as opposed to the parietal cortex when pathology is more evident at 4-5 months. Scale bar: 20 μm.

Chapter 3

Summary

In chapter 1, a novel bicistronic adeno-associated viral (AAV) vector was shown to be effective at prolonging life and ameliorating the neurodegenerative phenotype of cats with Sandhoff Disease (SD). Lifespan, *in vivo* biomarkers, enzyme activity, storage products, and markers of neuroinflammation, neurons, and myelin were all partially normalized relative to untreated SD controls. These metrics also indicated that the brainstem was the region with the mildest pathology after AAV treatment, along with the spinal cord when included. New pathology emerged in AAV-treated SD cats that lived longer than the 4-5 months of their untreated counterparts. The most notable was spinal cord compression, which led to the humane endpoint for 5/8 AAV-treated long-term cats, but storage products, neuroinflammation markers, and neuronal numbers also deviated more from normal in the long-term cohort than the short-term.

Evidence of a dose-dependent effect was apparent in lifespan differences (tripled for high dose, doubled for low dose compared to untreated SD cats) as well as the fact that the high dose long-term cohort had less storage and neuroinflammation than the low dose long-term cohort despite living 4 months longer. However, this effect could be partially due to vector batch variation, since all 4 cats in the low-dose long-term group were treated with vector from a batch that did not perform as well in 2 low-dose short-term cats. Though improving the details of vector preparation, design, and delivery are always a priority for gene therapy treatment destined for children, this study advances the field by demonstrating that IV delivery of a bicistronic AAV9 vector is effective in SD cats.

In chapter 2, myelin deficits were characterized in SD cats on an mRNA and protein level, and shown to be developing at a pre-symptomatic age (1 month). Baseline values for normal and SD cats were established for 5 mRNA markers at 4 different stages of feline development, and oligodendrocyte and myelin presence was determined at 3 different stages. As previously reported in humans and mice, the feline brainstem was one of the first areas to become myelinated in normal cats. This leads to the hypothesis that the brainstem in SD cats experiences a “delayed” myelination phenomenon before the neurodegenerative pathogenesis becomes severe and starts to destroy any abnormal myelin that has had a chance to form. This study underscores the importance of intervening with AAV treatment as early as possible, though the diagnosis of pre-symptomatic children is rare.

When considered in tandem, the results of these two chapters lead to the conclusion that early myelinating regions are best-corrected by AAV treatment. Though there is currently no evidence of a causative effect, there are several reasons why this is a promising avenue of investigation. For example, there is considerable overlap between major components of myelin sheaths and the storage products that accumulate in SD, such as cholesterol. Lysosomal dysfunction could lead to inefficient catabolism and metabolism pathways that are necessary for myelinogenesis. The formation of the myelin sheaths is an energetically expensive and complicated process, so perhaps reaching mid/end-stage pathology in the beginning of the myelination process (as occurs in later-myelinating regions) is more catastrophic than reaching it after there has been more time for myelin to form (as in early-myelinating regions). In this case, there would be fewer deficits in the early-myelinating regions (such as the brainstem) to “correct” with AAV treatment. This is supported by the observations in this study that pathology in the brainstem of untreated SD cats is typically less dramatic compared to the normal phenotype than the later-myelinating regions. Though eventually SD pathology becomes so severe that demyelination occurs, there is also evidence from this and previous studies that myelin sheaths form improperly in the first place (dysmyelinogenesis). Future studies that investigate overlap between normal myelination and the catabolism pathways affected by SD would provide more answers to these unanswered questions. Though it is challenging for researchers to investigate normal developmental processes in the face of neurodegenerative diseases, these studies are crucial to the refinement of gene therapy that will provide hope for the future for patients and their families.

References

1 Meikle, P. J., Hopwood, J. J., Clague, A. E. & Carey, W. F. Prevalence of Lysosomal Storage Disorders. *JAMA* **281**, 249-254, doi:10.1001/jama.281.3.249 (1999).

2 Nasrabady, S. E., Rizvi, B., Goldman, J. E. & Brickman, A. M. White matter changes in Alzheimer's disease: a focus on myelin and oligodendrocytes. *Acta Neuropathologica Communications* **6**, doi:10.1186/s40478-018-0515-3 (2018).

3 Luo, C., Song, W., Chen, Q., Yang, J., Gong, Q. & Shang, H.-F. White matter microstructure damage in tremor-dominant Parkinson's disease patients. *Neuroradiology* **59**, 691-698, doi:10.1007/s00234-017-1846-7 (2017).

4 Buccinnà, B., Piccinini, M., Prinetti, A., Scandroglio, F., Prioni, S., Valsecchi, M., Votta, B., Grifoni, S., Lupino, E., Ramondetti, C., Schuchman, E., Giordana, M., Sonnino, S. & Rinaudo, M. Alterations of myelin-specific proteins and sphingolipids characterize the brains of acid sphingomyelinase-deficient mice, an animal model of Niemann-Pick disease type A. *Journal of Neurochemistry* (2009).

5 Takikita, S., Fukuda, T., Mohri, I., Yagi, T. & Suzuki, K. Perturbed Myelination Process of Premyelinating Oligodendrocyte in Niemann-Pick Type C Mouse. *Journal of Neuropathology and Experimental Neurology* **63**, 660-673, doi:10.1093/jnen/63.6.660 (2004).

6 Provenzale, J. M., Nestrasil, I., Chen, S., Kan, S.-H., Le, S. Q., Jens, J. K., Snella, E. M., Vondrak, K. N., Yee, J. K., Vite, C. H., Elashoff, D., Duan, L., Wang, R. Y., Ellinwood, N. M., Guzman, M. A., Shapiro, E. G. & Dickson, P. I. Diffusion tensor imaging and myelin composition analysis reveal abnormal myelination in corpus callosum of canine mucopolysaccharidosis I. *Experimental Neurology* **273**, 1-10, doi:10.1016/j.expneurol.2015.07.021 (2015).

7 Ferreira, C. R. & Gahl, W. A. Lysosomal storage diseases. *Translational Science of Rare Diseases* **2**, 1-71, doi:10.3233/TRD-160005 (2017).

8 Sandhoff, K. & Harzer, K. Gangliosides and Gangliosidoses: Principles of Molecular and Metabolic Pathogenesis. *Journal of Neuroscience* **33**, 10195-10208, doi:10.1523/jneurosci.0822-13.2013 (2013).

9 Mahuran, D. J. Biochemical consequences of mutations causing the GM2 gangliosidoses. *Biochimica et Biophysica Acta (BBA) - Molecular Basis of Disease* **1455**, 105-138, doi:https://doi.org/10.1016/S0925-4439(99)00074-5 (1999).

10 Mahuran, D. J. β-hexosaminidase: Biosynthesis and processing of the normal enzyme, and identification of mutations causing Jewish Tay-Sachs disease. *Clinical Biochemistry* **28**, 101-106, doi:https://doi.org/10.1016/0009-9120(95)00003-R (1995).

11 Lawson, C. & Martin, D. Animal models of GM2 gangliosidosis: utility and limitations. *The Application of Clinical Genetics* **Volume 9**, 111-120, doi:10.2147/tacg.s85354 (2016).

12 Bley, A. E., Giannikopoulos, O. A., Hayden, D., Kubilus, K., Tifft, C. J. & Eichler, F. S. Natural History of Infantile GM2 Gangliosidosis. *Pediatrics* **128**, e1233, doi:10.1542/peds.2011-0078 (2011).

13 Maegawa, G. H. B., Stockley, T., Tropak, M., Banwell, B., Blaser, S., Kok, F., Giugliani, R., Mahuran, D. & Clarke, J. T. R. The Natural History of Juvenile or Subacute GM2 Gangliosidosis: 21 New Cases and Literature Review of 134 Previously Reported. *Pediatrics* **118**, e1550, doi:10.1542/peds.2006-0588 (2006).

14 Solovyeva, V. V., Shaimardanova, A. A., Chulpanova, D. S., Kitaeva, K. V., Chakrabarti, L. & Rizvanov, A. A. New Approaches to Tay-Sachs Disease Therapy. *Frontiers in Physiology* **9**, 1663 (2018).

15 Wada, R., Tifft, C. J. & Proia, R. L. Microglial activation precedes acute neurodegeneration in Sandhoff disease and is suppressed by bone marrow transplantation. *Proceedings of the National Academy of Sciences* **97**, 10954, doi:10.1073/pnas.97.20.10954 (2000).

16 Jeyakumar, M., Thomas, R., Elliot-Smith, E., Smith, D. A., van der Spoel, A. C., d'Azzo, A., Hugh Perry, V., Butters, T. D., Dwek, R. A. & Platt, F. M. Central nervous system inflammation is a hallmark of pathogenesis in mouse models of GM1 and GM2 gangliosidosis. *Brain* **126**, 974-987, doi:10.1093/brain/awg089 (2003).

17 Utz, J. R. J., Crutcher, T., Schneider, J., Sorgen, P. & Whitley, C. B. Biomarkers of central nervous system inflammation in infantile and juvenile gangliosidoses. *Molecular Genetics and Metabolism* **114**, 274-280, doi:https://doi.org/10.1016/j.ymgme.2014.11.015 (2015).

18 Cork, L. C., Munnell, J. F., Lorenz, M. D., Murphy, J. V., Baker, H. J. & Rattazzi, M. C. GM2 ganglioside lysosomal storage disease in cats with beta-hexosaminidase deficiency. *Science* **196**, 1014, doi:10.1126/science.404709 (1977).

19 Baker, H. J., Reynolds, G. D., Walkley, S. U., Cox, N. R. & Baker, G. H. The Gangliosidoses: Comparative Features and Research Applications. *Veterinary Pathology* **16**, 635-649, doi:10.1177/030098587901600602 (1979).

20 Martin, D. R., Krum, B. K., Varadarajan, G. S., Hathcock, T. L., Smith, B. F. & Baker, H. J. An inversion of 25 base pairs causes feline GM2 gangliosidosis variant 0. *Experimental Neurology* **187**, 30-37, doi:https://doi.org/10.1016/j.expneurol.2004.01.008 (2004).

21 Bradbury, A. M., Gray-Edwards, H. L., Shirley, J. L., McCurdy, V. J., Colaco, A. N., Randle, A. N., Christopherson, P. W., Bird, A. C., Johnson, A. K., Wilson, D. U., Hudson, J. A., De Pompa, N. L., Sorjonen, D. C., Brunson, B. L., Jeyakumar, M., Platt, F. M., Baker, H. J., Cox, N. R., Sena-Esteves, M. & Martin, D. R. Biomarkers for disease progression and AAV therapeutic efficacy in feline Sandhoff disease. *Experimental Neurology* **263**, 102-112, doi:10.1016/j.expneurol.2014.09.020 (2015).

22 McCurdy, V. J., Rockwell, H. E., Arthur, J. R., Bradbury, A. M., Johnson, A. K., Randle, A. N., Brunson, B. L., Hwang, M., Gray-Edwards, H. L., Morrison, N. E., Johnson, J. A., Baker, H. J., Cox, N. R., Seyfried, T. N., Sena-Esteves, M. & Martin, D. R. Widespread correction of central nervous system disease after intracranial gene therapy in a feline model of Sandhoff disease. *Gene Therapy* **22**, 181-189, doi:10.1038/gt.2014.108 (2015).

23 Rockwell, H. E., McCurdy, V. J., Eaton, S. C., Wilson, D. U., Johnson, A. K., Randle, A. N., Bradbury, A. M., Gray-Edwards, H. L., Baker, H. J., Hudson, J. A., Cox, N. R., Sena-Esteves, M., Seyfried, T. N. & Martin, D. R. AAV-mediated gene delivery in a feline model of Sandhoff disease corrects lysosomal storage in the central nervous system. *ASN Neuro* **7**, doi:10.1177/1759091415569908 (2015).

24 Bradbury, A. M., Peterson, T. A., Gross, A. L., Wells, S. Z., McCurdy, V. J., Wolfe, K. G., Dennis, J. C., Brunson, B. L., Gray-Edwards, H., Randle, A. N., Johnson, A. K., Morrison, E. E., Cox, N. R., Baker, H. J., Sena-Esteves, M. & Martin, D. R. AAV-mediated gene delivery attenuates neuroinflammation in feline Sandhoff disease. *Neuroscience* **340**, 117-125, doi:10.1016/j.neuroscience.2016.10.047 (2017).

25 Gray-Edwards, H. L., Brunson, B. L., Holland, M., Hespel, A.-M., Bradbury, A. M., McCurdy, V. J., Beadlescomb, P. M., Randle, A. N., Salibi, N., Denney, T. S., Beyers, R. J., Johnson, A. K., Voyles, M. L., Montgomery, R. D., Wilson, D. U., Hudson, J. A., Cox, N. R., Baker, H. J., Sena-Esteves, M. & Martin, D. R. Mucopolysaccharidosis-like phenotype in feline Sandhoff disease and partial correction after AAV gene therapy. *Molecular Genetics and Metabolism* **116**, 80-87, doi:10.1016/j.ymgme.2015.05.003 (2015).

26 Bergles, D. E. & Richardson, W. D. Oligodendrocyte Development and Plasticity. *Cold Spring Harbor Perspectives in Biology* **8** (2016).

27 Barateiro, A. & Fernandes, A. Temporal oligodendrocyte lineage progression: In vitro models of proliferation, differentiation and myelination. *Biochimica et Biophysica Acta (BBA) - Molecular Cell Research* **1843**, 1917-1929, doi:https://doi.org/10.1016/j.bbamcr.2014.04.018 (2014).

28 Nave, K.-A. & Trapp, B. D. Axon-Glial Signaling and the Glial Support of Axon Function. *Annual Review of Neuroscience* **31**, 535-561, doi:10.1146/annurev.neuro.30.051606.094309 (2008).

29 Saher, G., Brügger, B., Lappe-Siefke, C., Möbius, W., Tozawa, R.-i., Wehr, M. C., Wieland, F., Ishibashi, S. & Nave, K.-A. High cholesterol level is essential for myelin membrane growth. *Nature Neuroscience* **8**, 468-475, doi:10.1038/nn1426 (2005).

30 Feltri, M. A.-O., Weinstock, N. I., Favret, J., Dhimal, N., Wrabetz, L. & Shin, D. Mechanisms of demyelination and neurodegeneration in globoid cell leukodystrophy. . *Glia* (2021).

31 Kinney, H. C., Karthigasan, J., Borenshteyn, N. I., Flax, J. D. & Kirschner, D. A. Myelination in the developing human brain: Biochemical correlates. *Neurochemical Research* **19**, 983-996, doi:10.1007/BF00968708 (1994).

32 Almeida, R. G. & Lyons, D. A. On Myelinated Axon Plasticity and Neuronal Circuit Formation and Function. *The Journal of Neuroscience* **37**, 10023, doi:10.1523/JNEUROSCI.3185-16.2017 (2017).

33 Turner, R. Myelin and Modeling: Bootstrapping Cortical Microcircuits. *Frontiers in Neural Circuits* **13**, 34 (2019).

34 Chorghay, Z., Káradóttir, R. T. & Ruthazer, E. S. White Matter Plasticity Keeps the Brain in Tune: Axons Conduct While Glia Wrap. *Frontiers in Cellular Neuroscience* **12**, 428 (2018).

35 Folkerth, R. D. Abnormalities of Developing White Matter in Lysosomal Storage Diseases. *Journal of Neuropathology & Experimental Neurology* **58**, 887-902, doi:10.1097/00005072-199909000-00001 (1999).

36 Sargeant, T. J., Drage, D. J., Wang, S., Apostolakis, A. A., Cox, T. M. & Cachón-González, M. B. Characterization of Inducible Models of Tay-Sachs and Related Disease. *PLOS Genetics* **8**, e1002943, doi:10.1371/journal.pgen.1002943 (2012).

37 Kroll, R. A., Pagel, M. A., Roman-Goldstein, S., Barkovich, A. J., D'Agostino, A. N. & Neuwelt, E. A. White matter changes associated with feline GM2 gangliosidosis (Sandhoff disease): correlation of MR findings with pathologic and ultrastructural abnormalities. *AJNR Am J Neuroradiol* **16**, 1219-1226 (1995).

38 Kaye, E. M., Alroy, J., Raghavan, S. S., Schwarting, G. A., Adelman, L. S., Runge, V., Gelblum, D., Thalhammer, J. G. & Zuniga, G. Dysmyelinogenesis in animal model of GM1 gangliosidosis. *Pediatr Neurol* **8**, 255-261, doi:10.1016/0887-8994(92)90361-2 (1992).

39 Porter, B. F., Lewis, B. C., Edwards, J. F., Alroy, J., Zeng, B. J., Torres, P. A., Bretzlaff, K. N. & Kolodny, E. H. Pathology of GM2 Gangliosidosis in Jacob Sheep. *Veterinary Pathology* **48**, 807-813, doi:10.1177/0300985810388522 (2011).

40 Gray-Edwards, H. L., Maguire, A. S., Salibi, N., Ellis, L. E., Voss, T. L., Diffie, E. B., Koehler, J., Randle, A. N., Taylor, A. R., Brunson, B. L., Denney, T. S., Beyers, R. J., Gentry, A. S., Gross, A. L., Batista, A. R., Sena-Esteves, M. & Martin, D. R. 7T MRI Predicts Amelioration of Neurodegeneration in the Brain after AAV Gene Therapy. *Mol Ther Methods Clin Dev* **17**, 258-270, doi:10.1016/j.omtm.2019.11.023 (2020).

41 Folkerth, R. D., Alroy, J., Bhan, I. & Kaye, E. M. Infantile G(M1) gangliosidosis: complete morphology and histochemistry of two autopsy cases, with particular reference to delayed central nervous system myelination. *Pediatr Dev Pathol* **3**, 73-86, doi:10.1007/s100240050010 (2000).

42 Haberland, C., Brunngraber, E., Witting, L. & Brown, B. The white matter in GM2 gangliosidosis. *Acta Neuropathologica* **24**, 43-55, doi:10.1007/BF00691417 (1973).

43 Heinecke, K. A., Luoma, A., d'Azzo, A., Kirschner, D. A. & Seyfried, T. N. Myelin abnormalities in the optic and sciatic nerves in mice with GM1-Gangliosidosis. *ASN Neuro* **7**, 1-15, doi:10.1177/1759091415568913 (2015).

44 Broekman, M. L. D., Baek, R. C., Comer, L. A., Fernandez, J. L., Seyfried, T. N. & Sena-Esteves, M. Complete Correction of Enzymatic Deficiency and Neurochemistry in the GM1-gangliosidosis Mouse Brain by Neonatal Adeno-associated Virus–mediated Gene Delivery. *Molecular Therapy* **15**, 30-37, doi:10.1038/sj.mt.6300004 (2007).

45 Baek, R. C., Broekman, M. L. D., Leroy, S. G., Tierney, L. A., Sandberg, M. A., D'Azzo, A., Seyfried, T. N. & Sena-Esteves, M. AAV-Mediated Gene Delivery in Adult GM1-Gangliosidosis Mice Corrects Lysosomal Storage in CNS and Improves Survival. *PLOS One* **5**, e13468, doi:10.1371/journal.pone.0013468 (2010).

46 Baek, R. C., Martin, D. R., Cox, N. R. & Seyfried, T. N. Comparative analysis of brain lipids in mice, cats, and humans with Sandhoff disease. *Lipids* **44**, 197-205, doi:10.1007/s11745-008-3268-0 (2009).

47 Chakrabarti, A. K., Dasgupta, S., Gadsden, R. H., Hogan, E. L. & Banik, N. L. Regulation of brain m calpain Ca2+ sensitivity by mixtures of membrane lipids: activation at intracellular Ca2+ level. *J Neurosci Res* **44**, 374-380, doi:10.1002/(SICI)1097-4547(19960515)44:4<374::AID-JNR9>3.0.CO;2-9 (1996).

48 Gray-Edwards, H. L., Jiang, X., Randle, A. N., Taylor, A. R., Voss, T. L., Johnson, A. K., McCurdy, V. J., Sena-Esteves, M., Ory, D. S. & Martin, D. R. Lipidomic Evaluation of Feline Neurologic Disease after AAV Gene Therapy. *Molecular Therapy - Methods & Clinical Development* **6**, 135-142, doi:10.1016/j.omtm.2017.07.005 (2017).

49 van der Voorn, J. P., Kamphorst, W., van der Knaap, M. S. & Powers, J. M. The leukoencephalopathy of infantile GM1 gangliosidosis: oligodendrocytic loss and axonal dysfunction. *Acta Neuropathol* **107**, 539-545, doi:10.1007/s00401-004-0848-9 (2004).

50 Cachón-González, M. B., Wang, S. Z., Ziegler, R., Cheng, S. H. & Cox, T. M. Reversibility of neuropathology in Tay-Sachs-related diseases. *Hum Mol Genet* **23**, 730-748, doi:10.1093/hmg/ddt459 (2014).

51 Cummings, J., Wood, P., Walkley, S. U., De Lahunta, A. & DeForest, M. GM 2 gangliosidosis in a Japanese spaniel. *Acta neuropathologica* **67**, 247-253 (1985).

52 Walkley, S. U., Zervas, M. & Wiseman, S. Gangliosides as Modulators of Dendritogenesis in Normal and Storage Disease-affected Pyramidal Neurons. *Cerebral Cortex* **10**, 1028-1037, doi:10.1093/cercor/10.10.1028 (2000).

53 Sanders, D. N., Zeng, R., Wenger, D. A., Johnson, G. S., Johnson, G. C., Decker, J. E., Katz, M. L., Platt, S. R. & O'Brien, D. P. GM2 gangliosidosis associated with a HEXA missense mutation in Japanese Chin dogs: A potential model for Tay Sachs disease. *Molecular Genetics and Metabolism* **108**, 70-75, doi:10.1016/j.ymgme.2012.11.008 (2013).

54 Sargeant, T. J., Wang, S., Bradley, J., Smith, N. J. C., Raha, A. A., McNair, R., Ziegler, R. J., Cheng, S. H., Cox, T. M. & Cachon-Gonzalez, M. B. Adeno-associated virus-mediated expression of -hexosaminidase prevents neuronal loss in the Sandhoff mouse brain. *Human Molecular Genetics* **20**, 4371-4380, doi:10.1093/hmg/ddr364 (2011).

55 Suzuki, K. & Taniike, M. Murine model of genetic demyelinating disease: The twitcher mouse. *Microscopy Research and Technique* **32**, 204-214, doi:https://doi.org/10.1002/jemt.1070320304 (1995).

56 Vanier, M. T. & Svennerholm, L. CHEMICAL PATHOLOGY OF KRABBE'S DISEASE I. Lipid Composition and Fatty Acid Patterns of Phosphoglycerides in Brain. *Acta Paediatrica* **63**, 494-500, doi:https://doi.org/10.1111/j.1651-2227.1974.tb04838.x (1974).

57 Snook, E. R., Fisher-Perkins, J. M., Sansing, H. A., Lee, K. M., Alvarez, X., MacLean, A. G., Peterson, K. E., Lackner, A. A. & Bunnell, B. A. Innate Immune Activation in the Pathogenesis of a Murine Model of Globoid Cell Leukodystrophy. *The American Journal of Pathology* **184**, 382-396, doi:https://doi.org/10.1016/j.ajpath.2013.10.011 (2014).

58 Massaro, G., Geard, A. F., Liu, W., Coombe-Tennant, O., Waddington, S. N., Baruteau, J., Gissen, P. & Rahim, A. A. Gene Therapy for Lysosomal Storage Disorders: Ongoing Studies and Clinical Development. *Biomolecules* **11**, doi:10.3390/biom11040611 (2021).

59 Daya, S. & Berns Kenneth, I. Gene Therapy Using Adeno-Associated Virus Vectors. *Clinical Microbiology Reviews* **21**, 583-593, doi:10.1128/CMR.00008-08 (2008).

60 Lahey, H. G., Webber, C. J., Golebiowski, D., Izzo, C. M., Horn, E., Taghian, T., Rodriguez, P., Batista, A. R., Ellis, L. E., Hwang, M., Martin, D. R., Gray-Edwards, H. & Sena-Esteves, M. Pronounced Therapeutic Benefit of a Single Bidirectional AAV Vector Administered Systemically in Sandhoff Mice. *Molecular Therapy* (2020).

61 Bradbury, A. M., Gurda, B. L., Casal, M. L., Ponder, K. P., Vite, C. H. & Haskins, M. E. A review of gene therapy in canine and feline models of lysosomal storage disorders. *Hum Gene Ther Clin Dev* **26**, 27-37, doi:10.1089/humc.2015.002 (2015).

62 Kelly, J. M., Bradbury, A., Martin, D. R. & Byrne, M. E. Emerging therapies for neuropathic lysosomal storage disorders. *Progress in Neurobiology* **152**, 166-180, doi:10.1016/j.pneurobio.2016.10.002 (2017).

63 Rha, A. K., Maguire, A. S. & Martin, D. R. GM1 gangliosidosis: mechanisms and management. *The Application of Clinical Genetics* **14**, 209-233 (2021).

64 Guidotti, J. E., Mignon, A., Haase, G., Caillaud, C., McDonell, N., Kahn, A. & Poenaru, L. Adenoviral Gene Therapy of the Tay-Sachs Disease in Hexosaminidase A-Deficient Knock-Out Mice. *Human Molecular Genetics* **8**, 831-838, doi:10.1093/hmg/8.5.831 (1999).

65 Takaura, N., Yagi, T., Maeda, M., Nanba, E., Oshima, A., Suzuki, Y., Yamano, T. & Tanaka, A. Attenuation of ganglioside GM1 accumulation in the brain of GM1 gangliosidosis mice by neonatal intravenous gene transfer. *Gene Therapy* **10**, 1487-1493, doi:10.1038/sj.gt.3302033 (2003).

66 Bourgoin, C., Emiliani, C., Kremer, E. J., Gelot, A., Tancini, B., Gravel, R. A., Drugan, C., Orlacchio, A., Poenaru, L. & Caillaud, C. Widespread distribution of β-hexosaminidase activity in the brain of a Sandhoff mouse model after coinjection of adenoviral vector and mannitol. *Gene Therapy* **10**, 1841-1849, doi:10.1038/sj.gt.3302081 (2003).

67 Kyrkanides, S., Miller, J. H., Brouxhon, S. M., Olschowka, J. A. & Federoff, H. J. β-hexosaminidase lentiviral vectors: transfer into the CNS via systemic administration. *Molecular Brain Research* **133**, 286-298, doi:10.1016/j.molbrainres.2004.10.026 (2005).

68 Kyrkanides, S., Miller, J.-N. H., Tallents, R. H., Brouxhon, S. M., Centola, G. M. & Olschowka, J. A. Intraperitoneal inoculation of Sandhoff mouse neonates with an HIV-1 based lentiviral vector exacerbates the attendant neuroinflammation and disease phenotype. *Journal of Neuroimmunology* **188**, 39-47, doi:10.1016/j.jneuroim.2007.05.010 (2007).

69 Cachon-Gonzalez, M. B., Wang, S. Z., Lynch, A., Ziegler, R., Cheng, S. H. & Cox, T. M. Effective gene therapy in an authentic model of Tay-Sachs-related diseases. *Proceedings of the National Academy of Sciences* **103**, 10373-10378, doi:10.1073/pnas.0603765103 (2006).

70 Cachón-González, M. B., Wang, S. Z., McNair, R., Bradley, J., Lunn, D., Ziegler, R., Cheng, S. H. & Cox, T. M. Gene Transfer Corrects Acute GM2 Gangliosidosis—Potential Therapeutic Contribution of Perivascular Enzyme Flow. *Molecular Therapy* **20**, 1489-1500, doi:10.1038/mt.2012.44 (2012).

71 Bradbury, A. M., Cochran, J. N., McCurdy, V. J., Johnson, A. K., Brunson, B. L., Gray-Edwards, H., Leroy, S. G., Hwang, M., Randle, A. N., Jackson, L. S., Morrison, N. E., Baek, R. C., Seyfried, T. N., Cheng, S. H., Cox, N. R., Baker, H. J., Cachón-González, M. B., Cox, T. M., Sena-Esteves, M. & Martin, D. R. Therapeutic Response in Feline Sandhoff Disease Despite Immunity to Intracranial Gene Therapy. *Molecular Therapy* **21**, 1306-1315, doi:10.1038/mt.2013.86 (2013).

72 McCurdy, V. J., Johnson, A. K., Gray-Edwards, H. L., Randle, A. N., Brunson, B. L., Morrison, N. E., Salibi, N., Johnson, J. A., Hwang, M., Beyers, R. J., Leroy, S. G., Maitland, S., Denney, T. S., Cox, N. R., Baker, H. J., Sena-Esteves, M. & Martin, D. R. Sustained Normalization of Neurological Disease after Intracranial Gene Therapy in a Feline Model. *Science Translational Medicine* **6**, 231ra248-231ra248, doi:10.1126/scitranslmed.3007733 (2014).

73 Gray-Edwards, H. L., Randle, A. N., Maitland, S. A., Benatti, H. R., Hubbard, S. M., Canning, P. F., Vogel, M. B., Brunson, B. L., Hwang, M., Ellis, L. E., Bradbury, A. M., Gentry, A. S., Taylor, A. R., Wooldridge, A. A., Wilhite, D. R., Winter, R. L., Whitlock, B. K., Johnson, J. A., Holland, M., Salibi, N., Beyers, R. J., Sartin, J. L., Denney, T. S., Cox, N. R., Sena-Esteves, M. & Martin, D. R. Adeno-Associated Virus Gene Therapy in a Sheep Model of Tay–Sachs Disease. *Human Gene Therapy* **29**, 312-326, doi:10.1089/hum.2017.163 (2018).

74 Taghian, T., Marosfoi, M. G., Puri, A. S., Cataltepe, O. I., King, R. M., Diffie, E. B., Maguire, A. S., Martin, D. R., Fernau, D., Batista, A. R., Kuchel, T., Christou, C., Perumal, R., Chandra, S., Gamlin, P. D.,

Bertrand, S. G., Flotte, T. R., McKenna-Yasek, D., Tai, P. W. L., Aronin, N., Gounis, M. J., Sena-Esteves, M. & Gray-Edwards, H. L. A Safe and Reliable Technique for CNS Delivery of AAV Vectors in the Cisterna Magna. *Molecular Therapy* **28**, 411-421, doi:https://doi.org/10.1016/j.ymthe.2019.11.012 (2020).

75 Regier, D. S., Kwon, H. J., Johnston, J., Golas, G., Yang, S., Wiggs, E., Latour, Y., Thomas, S., Portner, C., Adams, D., Vezina, G., Baker, E. H. & Tifft, C. J. MRI/MRS as a surrogate marker for clinical progression in GM1 gangliosidosis. *American Journal of Medical Genetics* **170**, 634-644, doi:10.1002/ajmg.a.37468 (2016).

76 Gray-Edwards, H. L., Regier, D. S., Shirley, J. L., Randle, A. N., Salibi, N., Thomas, S. E., Latour, Y. L., Johnston, J., Golas, G., Maguire, A. S., Taylor, A. R., Sorjonen, D. C., McCurdy, V. J., Christopherson, P. W., Bradbury, A. M., Beyers, R. J., Johnson, A. K., Brunson, B. L., Cox, N. R., Baker, H. J., Denney, T. S., Sena-Esteves, M., Tifft, C. J. & Martin, D. R. Novel Biomarkers of Human GM1 Gangliosidosis Reflect the Clinical Efficacy of Gene Therapy in a Feline Model. *Molecular Therapy*, doi:10.1016/j.ymthe.2017.01.009 (2017).

77 Powell, S. K., Khan, N., Parker, C. L., Samulski, R. J., Matsushima, G., Gray, S. J. & McCown, T. J. Characterization of a novel adeno-associated viral vector with preferential oligodendrocyte tropism. *Gene therapy* **23**, 807-814, doi:10.1038/gt.2016.62 (2016).

78 Sandhoff, K., Harzer, K., Wässle, W. & Jatzkewitz, H. ENZYME ALTERATIONS AND LIPID STORAGE IN THREE VARIANTS OF TAY-SACHS DISEASE. *Journal of Neurochemistry* **18**, 2469-2489, doi:10.1111/j.1471-4159.1971.tb00204.x (1971).

79 Broekman, M. L. D., Tierney, L. A., Benn, C., Chawla, P., Cha, J. H. & Sena-Esteves, M. Mechanisms of distribution of mouse β-galactosidase in the adult GM1-gangliosidosis brain. *Gene Therapy* **16**, 303-308, doi:10.1038/gt.2008.149 (2009).

80 Weismann, C. M., Ferreira, J., Keeler, A. M., Su, Q., Qui, L., Shaffer, S. A., Xu, Z., Gao, G. & Sena-Esteves, M. Systemic AAV9 gene transfer in adult GM1 gangliosidosis mice reduces lysosomal storage in CNS and extends lifespan. *Human Molecular Genetics* **24**, 4353-4364, doi:10.1093/hmg/ddv168 (2015).

81 Walia, J. S., Altaleb, N., Bello, A., Kruck, C., Lafave, M. C., Varshney, G. K., Burgess, S. M., Chowdhury, B., Hurlbut, D., Hemming, R., Kobinger,

G. P. & Triggs-Raine, B. Long-Term Correction of Sandhoff Disease Following Intravenous Delivery of rAAV9 to Mouse Neonates. *Molecular Therapy* **23**, 414-422, doi:10.1038/mt.2014.240 (2015).

82 Tropak, M. B., Yonekawa, S., Karumuthil-Melethil, S., Thompson, P., Wakarchuk, W., Gray, S. J., Walia, J. S., Mark, B. L. & Mahuran, D. Construction of a hybrid β-hexosaminidase subunit capable of forming stable homodimers that hydrolyze GM2 ganglioside in vivo. *Molecular Therapy - Methods & Clinical Development* **3**, 15057, doi:10.1038/mtm.2015.57 (2016).

83 McCurdy, V. J., Johnson, A. K., Gray-Edwards, H. L., Randle, A. N., Bradbury, A. M., Morrison, N. E., Hwang, M., Baker, H. J., Cox, N. R., Sena-Esteves, M. & Martin, D. R. Therapeutic benefit after intracranial gene therapy delivered during the symptomatic stage in a feline model of Sandhoff disease. *Gene Therapy* **28**, 142-154, doi:10.1038/s41434-020-00190-1 (2021).

84 Maguire, A. S., Woodie, L. N., Judd, R. L., Martin, D. R., Greene, M. W. & Graff, E. C. Whole-slide image analysis outperforms micrograph acquisition for adipocyte size quantification. *Adipocyte* **9**, 567-575, doi:10.1080/21623945.2020.1823139 (2020).

85 Bankhead, P., Loughrey, M. B., Fernández, J. A., Dombrowski, Y., McArt, D. G., Dunne, P. D., McQuaid, S., Gray, R. T., Murray, L. J., Coleman, H. G., James, J. A., Salto-Tellez, M. & Hamilton, P. W. QuPath: Open source software for digital pathology image analysis. *Scientific Reports* **7**, 16878, doi:10.1038/s41598-017-17204-5 (2017).

86 Horovitz, D. D. G., Magalhães, T. d. S. P. C., e Costa, A. P., Carelli, L. E., e Silva, D. S., de Linhares e Riello, A. P. F. & Llerena, J. C. Spinal cord compression in young children with type VI mucopolysaccharidosis. *Molecular Genetics and Metabolism* **104**, 295-300, doi:https://doi.org/10.1016/j.ymgme.2011.07.019 (2011).

87 Tackley, G., Kong, Y., Minne, R., Messina, S., Winkler, A., Cavey, A., Everett, R., DeLuca, G. C., Weir, A., Craner, M., Tracey, I., Palace, J., Stagg, C. J. & Emir, U. An In-vivo 1H-MRS short-echo time technique at 7T: Quantification of metabolites in chronic multiple sclerosis and neuromyelitis optica brain lesions and normal appearing brain tissue. *Neuroimage* (2021).

88 Cai, Y., Xingming;, Z., Wang, Y., Yang, J., Zhao, Z., Fei, Z., Zhang, L., Gu, H. & Yang, T. Predictive value of magnetic resonance spectroscopy

combined with diffusion weighted imaging in patients with secondary brain insult after spontaneous intra-cerebral hemorrhage. *Zhonghua Wei Zhong Bing Ji Jiu Yi Xue* **32**, 1336-1339 (2020).

89 Bembi, B., Marchetti, F., Guerci, V. I., Ciana, G., Addobbati, R., Grasso, D., Barone, R., Cariati, R., Fernandez-Guillen, L., Butters, T. & Pittis, M. G. Substrate reduction therapy in the infantile form of Tay-Sachs disease. *Neurology* **66**, 278, doi:10.1212/01.wnl.0000194225.78917.de (2006).

90 Aronson, S. M., Saifer, A., Kanof, A., Volk, B. W. & B.S, P. Progression of amaurotic family idiocy as reflected by serum and cerebrospinal fluid changes. *The American Journal of Medicine* **24**, 390-401, doi:https://doi.org/10.1016/0002-9343(58)90325-5 (1958).

91 Satoh, H., Yamato, O., Asano, T., Yonemura, M., Yamauchi, T., Hasegawa, D., Orima, H., Arai, T., Yamasaki, M. & Maede, Y. Cerebrospinal fluid biomarkers showing neurodegeneration in dogs with GM1 gangliosidosis: possible use for assessment of a therapeutic regimen. *Brain Res* **1133**, 200-208, doi:10.1016/j.brainres.2006.11.039 (2007).

92 Quaglia, A., Karlsson, M., Larsson, M., Taylor, W. R., Diep, N. T. N., Trinh, D. T., Trung, N. V., Van Kinh, N. & Wertheim, H. F. L. Total lactate dehydrogenase in cerebrospinal fluid for identification of bacterial meningitis. *Journal of Medical Microbiology* **62**, 1772-1773, doi:https://doi.org/10.1099/jmm.0.058156-0 (2013).

93 Pekny, M. & Nilsson, M. Astrocyte activation and reactive gliosis. *Glia* **50**, 427-434, doi:10.1002/glia.20207 (2005).

94 Hirsch, E. C., Vyas, S. & Hunot, S. Neuroinflammation in Parkinson's disease. *Parkinsonism & Related Disorders* **18**, S210-S212, doi:https://doi.org/10.1016/S1353-8020(11)70065-7 (2012).

95 Eikelenboom, P., Bate, C., Van Gool, W. A., Hoozemans, J. J., Rozemuller, J. M., Veerhuis, R. & Williams, A. Neuroinflammation in Alzheimer's disease and prion disease. *Glia* **40**, 232-239, doi:10.1002/glia.10146 (2002).

96 Pringle, N. P., Mudhar, H. S., Collarini, E. J. & Richardson, W. D. PDGF receptors in the rat CNS: during late neurogenesis, PDGF alpha-receptor expression appears to be restricted to glial cells of the oligodendrocyte lineage. *Development* **115**, 535-551, doi:10.1242/dev.115.2.535 (1992).

97 Nishiyama, A., Lin, X.-H., Giese, N., Heldin, C.-H. & Stallcup, W. B. Interaction between NG2 proteoglycan and PDGF α-receptor on O2A progenitor cells is required for optimal response to PDGF. *Journal of Neuroscience Research* **43**, 315-330, doi:https://doi.org/10.1002/(SICI)1097-4547(19960201)43:3<315::AID-JNR6>3.0.CO;2-M (1996).

98 Laursen, L. S., Chan, C. W. & ffrench-Constant, C. Translation of myelin basic protein mRNA in oligodendrocytes is regulated by integrin activation and hnRNP-K. *Journal of Cell Biology* **192**, 797-811, doi:10.1083/jcb.201007014 (2011).

99 Lu, Q. R., Sun, T., Zhu, Z., Ma, N., Garcia, M., Stiles, C. D. & Rowitch, D. H. Common Developmental Requirement for Olig Function Indicates a Motor Neuron/Oligodendrocyte Connection. *Cell* **109**, 75-86, doi:10.1016/S0092-8674(02)00678-5 (2002).

100 Mei, F., Wang, H., Liu, S., Niu, J., Wang, L., He, Y., Etxeberria, A., Chan, J. R. & Xiao, L. Stage-Specific Deletion of Olig2 Conveys Opposing Functions on Differentiation and Maturation of Oligodendrocytes. *The Journal of Neuroscience* **33**, 8454-8462, doi:10.1523/jneurosci.2453-12.2013 (2013).